Development of Affinity Monoliths in 3D Printed Microfluidic Devices for Extraction of Preterm Birth Biomarkers

Ellen Kelsey Parker

A thesis submitted to the faculty of
Brigham Young University
in partial fulfillment of the requirements for the degree of

Master of Science

Adam T. Woolley, Chair
Steven R. Goates
Gregory Nordin

Department of Chemistry and Biochemistry

Brigham Young University

ABSTRACT

Development of Affinity Monoliths in 3D Printed Microfluidic Devices
for Extraction of Preterm Birth Biomarkers

Ellen Kelsey Parker
Department of Chemistry and Biochemistry, BYU
Master of Science

Preterm birth (PTB) is defined as birth before the 37th week of pregnancy and affects 15 million infants per year. Presently, there is no clinical test to determine PTB risk. A 3D printed microfluidic device is being developed as a clinical test for PTB risk via detection of a panel of biomarkers. A significant step is extraction of the PTB biomarkers from blood serum. In this work, I developed 3D printed microfluidic devices in which monoliths can be polymerized. Using the monolith as a solid support to attach antibody, I show that ferritin, one of the PTB biomarkers, can be selectively extracted from human blood serum. This is the first study where a monolith has been formed in a 3D printed microfluidic device and used to perform an immunoaffinity extraction. This work is an important step in developing a clinical test for PTB risk. The realization of this work also demonstrates that 3D printing can be used to fabricate functional microfluidic devices.

Keywords: 3D printing, microfluidics, affinity monolith, preterm birth

ACKNOWLEDGEMENTS

First I would like to thank my parents for always pushing me to do my best and for always believing in me, even when I didn't believe in myself. Thank you for teaching me that getting an education is important and for being an example to me of hard work. Most importantly thank you for listening to me talk about science even when you didn't understand. I likewise want to thank my sister Hannah for being there for me and helping me to remember to have fun. I am also very grateful to all my family and friends for always supporting me.

In addition, I would like to thank my advisor Dr. Adam Woolley for letting me join his lab as an undergrad and continue in his lab to get my Masters. I am so grateful for his patience with me and for being such a great example to me. Thank you for encouraging me to keep going even when things were not working and for answering my many questions. I am also very grateful for my other committee members Dr. Greg Nordin and Dr. Steven Goates. Thank you Dr. Nordin for your positivity in the face of challenges and for always reminding me that I should be excited about the science I am doing. Dr Goates, I have known you almost my whole time here at BYU and I am so grateful that even though you haven't always been my professor you are always there to give me advice and more importantly make me laugh. I also must thank the Woolley and Nordin lab groups for letting me bounce ideas off them, encouraging me, and being my friends. I would also like to thank all the professors and staff in the Department of Chemistry and Biochemistry for their support and help in my education. Furthermore, I would like to express appreciation to the Department of Chemistry and Biochemistry and the National Institute of Health for funding.

TABLE OF CONTENTS

ABSTRACT ii

ACKNOWLEDGEMENTS iii

LIST OF FIGURES vii

LIST OF TABLES ix

1. INTRODUCTION 1

1.1 Preterm Birth 1

1.2 Point of Care Tests 1

1.3 Monoliths 3

1.4 Microfluidics or Lab on a Chip 4

1.5 3D Printing 5

1.6 Objective and Significance of this Research Study 8

1.7 Thesis Overview 8

1.8 References 9

2. MATERIALS AND METHODS 13

2.1 Materials and Reagents 13

2.2 3D Printing 14

2.2.1 Glass Slide Preparation 14

2.2.2 Resin Preparation 15

2.2.3 Description of 3D Printing Designs 15

2.2.4 Edge Compensation 16

2.2.5 Water Contact Angle 16

2.2.6 Device Stability 17
2.3 Monolith Preparation 18
2.3.1 SEM 19
2.4 Antibody Characterization and Immobilization 19
2.5 Sample Preparation 20
2.6 Experimental Setup 21
2.7 Device Operation 22
2.8 References 23
3. RESULTS AND DISCUSSION 24
3.1 3D Printed Device Properties 24
3.1.1 Water Contact Angle 24
3.1.2 Edge Compensation 25
3.1.3 Post Exposure 27
3.2 Device Designs 28
3.2.1 Initial Device Design 28
3.2.2 Improved Device Design 29
3.3 Monoliths 30
3.3.1 Initial Monolith Formulation 30
3.3.2 Improved Monolith Formulation 31
3.4 Antibodies 32
3.4.1 Attachment of Antibody to Monolith 32
3.4.2 Dot Blots 33
3.5 Establishing Experimental Conditions 34

3.5.1 Rinsing Buffer 34
3.5.2 Voltage 35
3.5.3 Vacuum vs Voltage 36
3.6 Extraction Experiments 37
3.6.1 Extraction of Lactoferrin 37
3.6.2 Extraction of Ferritin 39
3.6.3 Confirmation of Ferritin Selectivity 40
3.6.4 Extraction of Ferritin from a Human Blood Serum Sample 41
3.7 References 42
4. CONCLUSIONS AND FUTURE WORK 43
4.1 Conclusions 43
4.2 Future Work 43
4.3 References 45
Appendix 1 46
A 1.1 OpenSCAD Code for Initial Device Design 46
A 1.2 OpenScad Code for Improved Device Design 47
A 1.3 Representative Water Contact Angle Picture 48
A 1.4 Representative CCD Images for Extractions 48
A 1.4.1 Extraction of Ferritin 48
A 1.4.2 Confirmation of Ferritin Selectivity 49
A 1.4.3 Extraction of Ferritin from a Human Blood Sample 49

LIST OF FIGURES

Figure 1.1 Schematic of the traditional microfabrication of microfluidic devices 4

Figure 2.1 Stereolithographic 3D printing 14

Figure 2.2 Image of SCAD designs for 3D printed microfluidic devices 15

Figure 2.3 Image of SCAD design for test blocks with channels 17

Figure 2.4 Device operation schematic 22

Figure 3.1 Water contact angles of 3D printed material, PMMA, COC, and a glass slide before and after being exposed to 1 M HCl and 1 M NaOH 24

Figure 3.2 SEM images of test blocks with different edge exposure patterns 26

Figure 3.3 Side view images of block cracking taken with the profilometer 27

Figure 3.4. Photograph of the initial 3D printed microfluidic device design 28

Figure 3.5 Side view of monolith window cracking taken with the profilometer 29

Figure 3.6 Photograph of the improved 3D printed microfluidic device design 30

Figure 3.7. SEM images of monoliths formed in the initial device design with 10 minute exposure 31

Figure 3.8 SEM images of monoliths 1 and 2 made in devices with the improved design 32

Figure 3.9 Labeled antibody attachment 33

Figure1 3.10 Dot blots of (A) ferritin and antiferritin and (B) lactoferrin and antilactoferrin 34

Figure 3.11. Fluorescent spectra of 1 μM Alexa Fluor 532 in 20 mM phosphate pH 7 and 20 mM HEPES pH 7 35

Figure 3.12. Comparison of observed current as a function of an applied voltage over time 36

Figure 3.13. CCD images of sample loading with (A) voltage and (B) vacuum 37

Figure 3.14 Elution after extraction of 5 μM lactoferrin on an unmodified monolith (control) and a monolith modified with anti-lactoferrin (antibody) in the initial (9 channel) device design..... 38
Figure 3.15 Immunoaffinity extraction of ferritin on both unmodified (control) and antiferritin modified monoliths 39
Figure 3.16. Extraction of 1 μM CRF on a monolith with (antiferritin) and without (control) antiferritin attached 40
Figure 3.17 Extraction of spiked serum on a monolith with (antiferritin) and without (control) antiferritin attached 41
Figure 4.1 Proposed design for automated immunoaffinity extraction 44

LIST OF TABLES

Table 2.1: Exposure Times for Each Layer in Test Block..... 18

1. INTRODUCTION

1.1 Preterm Birth

Preterm birth (PTB) is defined by the World Health Organization as birth before the 37th week of pregnancy.[1] Over 15 million preterm babies, or 1 in 10, are born each year worldwide.[2] One million of those babies die due to complications of PTB every year. The survivors face several health and developmental problems including cerebral palsy, chronic lung disease, vision and hearing loss, and intellectual impairment.[3-4]

It is believed that PTB is caused in part by activation of inflammatory gene expression in the myometrium, fetal membranes, and cervix or infection of the amniotic cavity.[5] These result in early contractions and eventually premature birth. Shots, often containing progesterone, can be administered to prevent or delay PTB.[6] However there is still more that can be learned about the causes of PTB and how it can be prevented.

One hurdle in fully understanding PTB is that currently there is no clinical test to predict PTB risk.[3] If one could predict PTB risk weeks before the contractions took place, more could be observed and understood about the underlying causes of PTB and more could be done to prevent it. Recently, Esplin and collaborators[7] evaluated 9 biomarkers that can predict PTB with 87% selectivity and 81% specificity. Using this panel of biomarkers, our group is working to make a point-of-care test (POCT) to predict PTB risk.

1.2 Point of Care Tests

A POCT is defined as a medical test at the time and place of patient care.[8] This is attractive because bringing the test to the patient has the potential to shorten turn-around times for test results.[9] Currently, most medical tests are performed and analyzed at a separate testing facility.

However, if testing could be done at home or right in the doctor's office via POCT, the patient's test results could be analyzed immediately after taking the test and the necessary treatment could immediately be administered. Thus, POCTs help to improve feedback rates in medical testing.

Because POCTs are designed to be done at the time and place of patient care they have the potential to solve important problems. Already there are some commercially available POCTs including home pregnancy tests and glucose monitors.[10] These POCTs have been proven useful in helping women to know if they are pregnant and in helping diabetes sufferers determine and manage their blood sugar levels. Researchers have also looked into using POCTs as a way to improve assessment and treatment of infectious diseases in developing countries where people don't always have access to a hospital.[11-12] Some researchers have even developed ways to use POCTs with smartphones so that data can be sent to a hospital for those who live far away.[13-14] Scientists have also looked into POCTs as a way to continually monitor those who are critically or chronically ill.[15] Thus, research into POCTs continues to expand as efforts are increased to bring healthcare to more people.

A POCT for PTB risk would be helpful because results could be immediately analyzed and preventive measures could be taken to help the baby reach full term. Currently, most hospital testing is done in a centralized lab that requires sample transport, sample preparation, and post analysis steps.[9] This increases the time between taking the test and receiving the results. Because PTB is often spontaneous, the sooner that the results are received the sooner preventive medical treatment can be implemented.[16] Thus, our group is working to develop a miniaturized platform that could be made into a POCT for PTB risk so those who are at risk for PTB get the preventive treatment they need more quickly.

1.3 Monoliths

An important aspect of POCTs is the need for simple and effective sample preparation because they often process complex biological matrices. Monoliths, continuous porous polymers that are used as stationary phases for liquid chromatography, are one such tool used in sample preparation. Monoliths have advantages over traditional packed columns because they have higher flow rates, lower back pressure, and reduced mass transfer resistance.[17-18] For these reasons monoliths are desirable in POCTs compared to traditional packed columns.

Another feature that makes monoliths useful is that they can be functionalized, for example, by chemically modifying unreacted functional groups already present in the pre-synthesized monolith such as epoxy, hydroxyl, or aldehyde groups.[19] Another way they can be functionalized is by incorporating prefunctionalized monomers into the monolith solution prior to polymerization. These functionalities have allowed monoliths to be used for a variety of applications including cation and anion exchange, metal ion affinity, and protein affinity separations.[20]

In addition to being able to be functionalized for a particular use, monoliths can also be scaled up for larger volume experiments or more importantly scaled down for smaller experiments.[20] They can be used for small scale applications because organic monoliths can be made *in situ* or inside the column by polymerizing a mixture of monomers, porogens, and a free radical initiator. Thus, even in small channels the liquid monolith solution can be flowed in and then polymerized to the size of the small channel. For this reason monoliths are often used in microfluidic applications.[21-22]

1.4 Microfluidics or Lab on a Chip

Microfluidics is defined as the science and technology of manipulating small volumes of liquid in channels with dimensions of tens to hundreds of micrometers.[23] The field of microfluidics began to emerge as the field of microelectronics expanded and new technologies allowed for smaller and smaller channels.[24] Since its emergence in the 1990s, microfluidics has been looked to as an important tool for fluid manipulation.

Microfluidics offers many advantages for designing fluid based assays. First using smaller volumes of liquid means that less sample or reagent is required and less waste is generated.[25-26] Second, the small size provides the capability to integrate many processes such as sample preparation and detection on the same chip earning microfluidics the nickname "lab on a chip".[27-28] Lastly, the small size means that that microfluidic devices are portable.[29] For these reasons microfluidics is an important tool in creating fluid based assays.

The biggest limitation of microfluidics is the fabrication of complex designs integrated with detailed 3D structures. The conventional fabrication of microfluidic devices uses techniques developed for microelectronics fabrication as seen in Figure 1.1. First a photomask design is

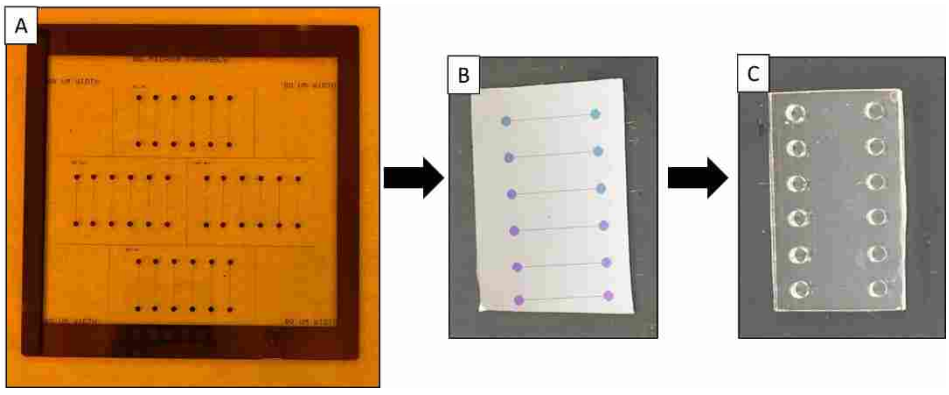

Figure 1.1 Schematic of the traditional microfabrication of microfluidic devices. *(A) Design and make photomask. (B) Silicon template made using photolithography. (C) Final device made by hot embossing the template design into plastic and thermal bonding layers together.*

made in a material such as glass or chromium from a digital design. Next, photolithography is used to pattern and etch the photomask design into a silicon template. Hot embossing of the silicon template into the plastic of choice transfers the features into the device material. Bonding is done to attach multiple layers (if necessary) making the 3D design from the 2D layers and sealing the channels. For simple designs such as the traditional "T-shape", this process has become automated and commercialized through injection molding or machining.[30-32] However for more complex designs that have multiple channels with pumps and valves or other 3D features, this process requires special equipment and trained professionals to ensure that all the layers are designed, fabricated, and aligned correctly.[33] Thus, the total process for making a complex microfluidic device from mask creation to device assembly can take a week even for a trained scientist. Additionally this process is resource intensive with many steps requiring a cleanroom environment and safety apparatus such as fume hoods, full length gloves, and face shields. For these reasons, the current fabrication method for complex microfluidic devices does not readily lend itself to commercialization and ultimately widespread implementation. Thus, many researchers including our group have looked to 3D printing as a means of overcoming this limitation for fabricating complex microfluidic devices.

1.5 3D Printing

3D printing is an additive manufacturing technique, which builds objects layer by layer.[34] With 3D printing, a computer design is made into a physical object in just one step. This has made it a common tool for rapid prototyping. 3D printing has already been used in a variety of fields including jewelry making, dentistry, and auto manufacturing.[35-36] The field is expected to grow as more applications are found for its ability to manufacture an object quickly.

3D printing offers several advantages over traditional microfabrication techniques for making complex microfluidic devices. First, from design to physical object a device can be made in less than 1 hour compared to a week needed to make a complex device using traditional microfabrication techniques.[34] Second, 3D printing is considerably cheaper than traditional microfabrication because you don't need cleanroom equipment to make the mask, do photolithography, and bond devices.[27] The only materials you need are a computer, the 3D printer, and the material you are going to print. Third, 3D printers are easier to use than the special equipment needed for traditional microfabrication, which makes 3D printing a microfabrication technique that can possibly be used in a commercial setting and made scalable for manufacturing. Finally, it is easier to make shapes in 3D because you do not need to align the 2D layers manually to create the 3D features.[34] Thus 3D printing has the potential to overcome the limitations of traditional microfabrication techniques for making complex microfluidic devices.

Several different types of 3D printers include: fused deposition modeling (FDM), polyjet, and stereolithographic. The FDM printer works by extruding a thermoplastic through a heated nozzle in patterned layers. When the thermoplastic cools, it hardens to form a solid object. A benefit of using a FDM printer is that one can use two or more different materials in the same print by having multiple nozzles.[37] Printing of enclosed features like a channel requires at least two materials, the printing material and a sacrificial support material to prevent collapse of the feature during the printing process. This makes it difficult to clear out small features because the solid support material has to be cleared out. In addition the features are limited in resolution by the nozzle size and the xy motor.[38] A polyjet printer uses a sprayer to deposit droplets of resin which are subsequently cured by a UV light. Each layer is deposited and cured on top of the

previous layer. As with FDM, more than one material can be used during printing.[39] However, similar to FDM, in order to form small, enclosed features, a support material is needed to hold the place of these features during printing. Because this support material is a solid, it is difficult to remove after printing. Polyjet printers have better resolution than FDM printers because the resolution is only limited by the size of the droplet.[40]

A stereolithographic printer uses a vat of liquid resin that is typically photopolymerized with an LED light patterned by a projector or a scanned laser which determines spatially where the polymerization occurs. In contrast to FDM or polyjet, the voids where the small features are formed are filled with unpolymerized liquid resin which makes them easier to clear out than solid support material. Another benefit of using a stereolithographic 3D printer is that the resin can be modified for the application as long as it is photopolymerizable by the light source.[41] Thus, both the light source and resin composition can be changed to achieve the desired properties. All of these types of 3D printers have allowed the field of 3D printing to grow and facilitate a variety of applications.

Already researchers have found some fluidic applications for 3D printed devices. For example, Breadmore et al.[42] used a 3D printer to make fluidic devices that are clear and can be used to monitor nitrate in tap water. Others have used 3D printed devices to perform micro free-flow electrophoresis of fluorescent dyes.[43] However most of these 3D printed fluidic channel sizes were not as small as what can be made by traditional microfabrication techniques.[40] In my research I am using a customized stereolithographic 3D printer to approach the feature sizes of devices made with traditional fabrication techniques.[44] This printer takes advantage of the stereolithographic features previously mentioned and has resolution that is sufficient to print 18

μm × 20 μm channels. With the ability to 3D print truly microfluidic channels, more applications for 3D printed devices can be realized.

1.6 Objective and Significance of this Research Study

I propose that preterm birth (PTB) risk can be determined using a 3D printed microfluidic device. The proposed microfluidic device has three parts: immunoaffinity extraction, on-chip labeling, and separation. I focus on optimizing the conditions for the immunoaffinity extraction module. This is the first demonstration of forming a monolith in a 3D printed device. It is also the first study where immunoaffinity extraction of PTB biomarkers has been performed in a 3D printed microfluidic device. The success of this research shows that 3D printing can be used as a fabrication technique for microfluidic devices and that immunoaffinity experiments can be carried out in them. Also, this work is an important cornerstone for developing a completely integrated 3D printed microfluidic device that can be used to test for PTB risk.

1.7 Thesis Overview

In this chapter, background is given on preterm birth, point of care tests, monoliths, microfluidics, and 3D printing.

In Chapter 2, the materials and methods used in this work are described. A custom-built 3D printer was used to fabricate the microfluidic devices. I developed an immunoaffinity method to extract the preterm birth biomarkers, using a glycidyl methacrylate monolith as the solid support to attach antibodies.

In Chapter 3, I report the results and discuss my work. I successfully formed monoliths in 3D printed microfluidic devices. I also showed the specific extraction of ferritin from human blood serum.

In Chapter 4, I present my conclusions and possible future directions for extension of my work to include the extraction of all nine PTB biomarkers. I also discuss the possibility of making a 3D printed device that contains pumps and valves so that the extraction of PTB biomarkers can be automated.

1.8 References

1. WHO | Preterm birth. http://www.who.int/mediacentre/factsheets/fs363/en/.

2. Preterm Birth | Maternal and Infant Health | Reproductive Health | CDC. https://www.cdc.gov/reproductivehealth/maternalinfanthealth/pretermbirth.htm.

3. Behrman, R. E.; Butler, A. S., *Preterm Birth: Causes, Consequences, and Prevention*. National Academies Press (US): Washington (DC), 2007.

4. Blencowe, H.; Cousens, S.; Oestergaard, M. Z.; Chou, D.; Moller, A.-B.; Narwal, R.; Adler, A.; Garcia, C. V.; Rohde, S.; Say, L.; Lawn, J. E., National, regional, and worldwide estimates of preterm birth rates in the year 2010 with time trends since 1990 for selected countries: a systematic analysis and implications. *The Lancet* **2012,** *379* (9832), 2162-2172.

5. Keelan, J. A., Intrauterine inflammatory activation, functional progesterone withdrawal, and the timing of term and preterm birth. *Journal of Reproductive Immunology* **2018,** *125*, 89-99.

6. Roberto, R.; Sudhansu, K. D.; Susan, J. F., Preterm labor: One syndrome, many causes. *Science* **2014,** *345* (6198), 760-765.

7. Esplin, M. S.; Merrell, K.; Goldenberg, R.; Lai, Y.; Iams, J. D.; Mercer, B.; Spong, C. Y.; Miodovnik, M.; Simhan, H. N.; van Dorsten, P.; Dombrowski, M., Proteomic identification of serum peptides predicting subsequent spontaneous preterm birth. *American Journal of Obstetrics and Gynecology* **2011,** *204* (5), 391.e8.

8. Paul, K. D.; Emily, P. H.; Farzad, N.; Kenneth, A. F.; Douglas, W.; William, B.; William, R.; Ingrid, V. B., Evaluating Diagnostic Point-of-Care Tests in Resource-Limited Settings. *The Lancet Infectious Diseases* **2014,** *14*, 239-249.

9. Quinn, A. D.; Dixon, D.; Meenan, B. J., Barriers to hospital-based clinical adoption of point-of-care testing (POCT): A systematic narrative review. *Critical Reviews in Clinical Laboratory Sciences* **2016,** *53* (1), 1-12.

10. Vashist, S. K.; Luppa, P. B.; Yeo, L. Y.; Ozcan, A.; Luong, J. H. T., Emerging Technologies for Next-Generation Point-of-Care Testing. *Trends in Biotechnology* **2015,** *33* (11), 692-705.

11. Chan, K.; Weaver, S. C.; Wong, P.-Y.; Lie, S.; Wang, E.; Guerbois, M.; Vayugundla, S. P.; Wong, S., Rapid, Affordable and Portable Medium-Throughput Molecular Device for Zika Virus. *Scientific Reports* **2016,** *6*, 38223.

12. Hou, Y.-H.; Wang, J.-J.; Jiang, Y.-Z.; Lv, C.; Xia, L.; Hong, S.-L.; Lin, M.; Lin, Y.; Zhang, Z.-L.; Pang, D.-W., A colorimetric and electrochemical immunosensor for point-of-care detection of enterovirus 71. *Biosensors and Bioelectronics* **2018,** *99*, 186-192.

13. Knowlton, S.; Joshi, A.; Syrrist, P.; Coskun, A. F.; Tasoglu, S., 3D-printed smartphone-based point of care tool for fluorescence- and magnetophoresis-based cytometry. *Lab Chip* **2017,** *17* (16), 2839-2851.

14. Liu, Y.; Chen, C.; Summers, S.; Medawala, W.; Spence, D. M., C-peptide and zinc delivery to erythrocytes requires the presence of albumin: implications in diabetes explored with a 3D-printed fluidic device. *Integrative Biology* **2015,** *7* (5), 534-543.

15. Luppa, P. B.; Müller, C.; Schlichtiger, A.; Schlebusch, H., Point-of-care testing (POCT): Current techniques and future perspectives. *Trends in Analytical Chemistry* **2011,** *30* (6), 887-898.

16. Campbell, S., Prevention of spontaneous preterm birth: universal cervical length assessment and vaginal progesterone in women with a short cervix: time for action! *American Journal of Obstetrics and Gynecology* **2018,** *218* (2), 151-158.

17. Andjelković, U.; Tufegdžić, S.; Popović, M., Use of monolithic supports for high-throughput protein and peptide separation in proteomics. *Electrophoresis* **2017,** *38* (22-23), 2851-2869.

18. Svec, F.; Lv, Y., Advances and recent trends in the field of monolithic columns for chromatography. *Analytical Chemistry* **2015,** *87* (1), 250.

19. Tetala, K. K. R.; Vijayalakshmi, M. A., A review on recent developments for biomolecule separation at analytical scale using microfluidic devices. *Analytica Chimica Acta* **2016,** *906*, 7-21.

20. Masini, J. C.; Svec, F., Porous monoliths for on-line sample preparation: A review. *Analytica Chimica Acta* **2017,** *964*, 24-44.

21. Knob, R.; Sahore, V.; Sonker, M.; Woolley, A. T., Advances in monoliths and related porous materials for microfluidics. *Biomicrofluidics* **2016,** *10*, 032901.

22. Dziomba, S.; Araya-Farias, M.; Smadja, C.; Taverna, M.; Carbonnier, B.; Tran, N. T., Solid supports for extraction and preconcentration of proteins and peptides in microfluidic devices: A review. *Analytica Chimica Acta* **2017,** *955*, 1-26.

23. Whitesides, G. M., The origins and the future of microfluidics. *Nature* **2006,** *442* (7101), 368.

24. Mark, D.; Haeberle, S.; Roth, G.; Stetten, F. v.; Zengerle, R., Microfluidic lab-on-a-chip platforms: requirements, characteristics and applications. *Chemical Society Reviews* **2010,** *39* (3), 1153-1182.

25. Chin, C. D.; Linder, V.; Sia, S. K., Commercialization of microfluidic point-of-care diagnostic devices. *Lab Chip* **2012,** *12*, 2118-2134.

26. Pandey, C.; Augustine, S.; Kumar, S.; Kumar, S.; Nara, S.; Srivastave, S.; Malhotra, B., Microfluidics based point-of-care diagnostics. *Biotechnology Journal* **2017,** *13* (1).

27. Ho, C. M. B.; Ng, S. H.; Li, K. H. H.; Yoon, Y.-J., 3D printed microfluidics for biological applications. *Lab Chip* **2015,** *15* (18), 3627-3637.

28. Hu, J.; Cui, X.; Gong, Y.; Xu, X.; Gao, B.; Wen, T.; Lu, T. J.; Xu, F., Portable microfluidic and smartphone-based devices for monitoring of cardiovascular diseases at the point of care. *Biotechnology Advances* **2016,** *34* (3), 305-320.

29. Nge, P. N.; Rogers, C. I.; Woolley, A. T., Advances in Microfluidic Materials, Functions, Integration, and Applications. *Chemical Reviews* **2013,** *113* (4), 2550-2583.

30. Duffy, C. F.; MacCraith, B.; Diamond, D.; O'Kennedy, R.; Arriaga, E. A., Fast electrophoretic analysis of individual mitochondria using microchip capillary electrophoresis with laser induced fluorescence detection. *Lab Chip* **2006,** *6* (8), 1007-1011.

31. Han, H. T.; Zheng, Z. X.; Pan, D. W.; Wang, C. C.; Hu, X. P.; Wang, Y. C., Portable microfluidic chip electrophoresis device with integrated Pt electrodes for the analysis of AgNPs. *Micro Nano Lett.* **2018,** *13* (3), 302-305.

32. Li, S. F. Y.; Kricka, L. J., Clinical analysis by microchip capillary electrophoresis. *Clin. Chem.* **2006,** *52* (1), 37-45.

33. Sahore, V.; Sonker, M.; Nielsen, A. V.; Knob, R.; Kumar, S.; Woolley, A. T., Automated microfluidic devices integrating solid-phase extraction, fluorescent labeling, and microchip electrophoresis for preterm birth biomarker analysis. *Analytical and Bioanalytical Chemistry* **2018,** *410* (3), 933-941.

34. Yazdi, A. A.; Popma, A.; Wong, W.; Nguyen, T.; Pan, Y.; Xu, J., 3D printing: an emerging tool for novel microfluidics and lab-on-a-chip applications. *Microfluidics and Nanofluidics* **2016,** *20* (3), 50.
35. Berman, B., 3-D printing: The new industrial revolution. *Business Horizons* **2012,** *55* (2), 155-162.

36. Stansbury, J. W.; Idacavage, M. J., 3D printing with polymers: Challenges among expanding options and opportunities. *Dental Materials* **2016,** *32* (1), 54-64.

37. Zhou, Y. F., The recent development and applications of fluidic channels by 3D printing. *J. Biomed. Sci.* **2017,** *24*, 22.

38. Chia, H. N.; Wu, B. M., Recent advances in 3D printing of biomaterials. *J. Biol. Eng.* **2015,** *9*, 14.

39. Bhattacharjee, N.; Urrios, A.; Kang, S.; Folch, A., The upcoming 3D-printing revolution in microfluidics. *Lab Chip* **2016,** *16* (10), 1720-1742.

40. Beauchamp, M. J.; Nordin, G. P.; Woolley, A. T., Moving from millifluidic to truly microfluidic sub-100-μm cross-section 3D printed devices. *Analytical and Bioanalytical Chemistry* **2017,** *409* (18), 4311-4319.

41. Gong, H.; Beauchamp, M.; Perry, S.; Woolley, A. T.; Nordin, G. P., Optical approach to resin formulation for 3D printed microfluidics. *RSC Adv.* **2015,** *5* (129), 106621-106632.

42. Shallan, A. I.; Smejkal, P.; Corban, M.; Guijt, R. M.; Breadmore, M. C., Cost-Effective Three-Dimensional Printing of Visibly Transparent Microchips within Minutes. *Analytical Chemistry* **2014,** *86* (6), 3124-3130.

43. Anciaux, S. K.; Geiger, M.; Bowser, M. T., 3D Printed Micro Free-Flow Electrophoresis Device. *Analytical Chemistry* **2016,** *88* (15), 7675-7682.

44. Gong, H.; Bickham, B. P.; Woolley, A. T.; Nordin, G. P., Custom 3D printer and resin for 18 μm × 20 μm microfluidic flow channels. *Lab Chip* **2017,** *17* (17), 2899-2909.

2. MATERIALS AND METHODS

2.1 Materials and Reagents

The following chemicals were ordered from Sigma (St. Louis, MO): 3-(trimethoxysilyl)propyl methacrylate, Tris hydrochloride, dimethyl sulfoxide (DMSO), lactoferrin, antilactoferrin, antiferritin, glycidyl methacrylate (GMA), ethylene glycol dimethacrylate (EGDMA), 1-dodecanol, 2,2-dimethoxy-2-phenylacetophenone (DMPA), and poly(ethylene glycol) diacrylate (PEGDA, MW 250). Sodium phosphate, sodium bicarbonate, sodium carbonate, boric acid, ferritin and Amicon ultra 0.5 mL centrifugal filters (3, 10, and 30 kDa cutoff) were all purchased from Millipore Sigma (Burlington, MA). All solutions were made with deionized water (18.3 MΩ cm) filtered by a Barnstead EASYpure UV/UF system (Dubuque, IA). 2-Propanol (IPA) and toluene were both purchased from Macron (Center Valley, PA). Acetone, Tris base, and Alexa Fluor 532 (carboxylic acid, succinimidyl ester) were purchased from Fisher Scientific (Fair Lawn, NJ). Sodium hydroxide (NaOH) and Tween 20 were purchased from Mallinckrodt Baker (Paris, KY). Glass slides for 3D printing were purchased from VWR (Radnor, PA). Cyclohexanol was purchased from Spectrum (New Brunswick, NJ), 2-nitrophenyl phenyl sulfide (NPS) was purchased from TCI (Portland, OR) and dry milk was purchased from Walmart (Bentonville, AR). Corticotropin releasing factor (CRF) was purchased from GeneScript (Piscataway, NJ). Female human blood serum (off-the-clot, sterile filtered) was purchased from Zen-Bio (Research Triangle Park, NC). Phenylbis(2,4,6-trimethylbenzoyl)phosphine oxide (Irgacure 819) was provided by BASF (Mississauga, ON). A Nanodrop ND-1000 spectrophotometer (Wilmington, DE) was used to look at fluorescence intensity.

2.2 3D Printing

A custom stereolithographic 3D printer was used to create microfluidic devices as described previously[1] and seen in Figure 2.1. This printer uses a 385 nm light source and has a

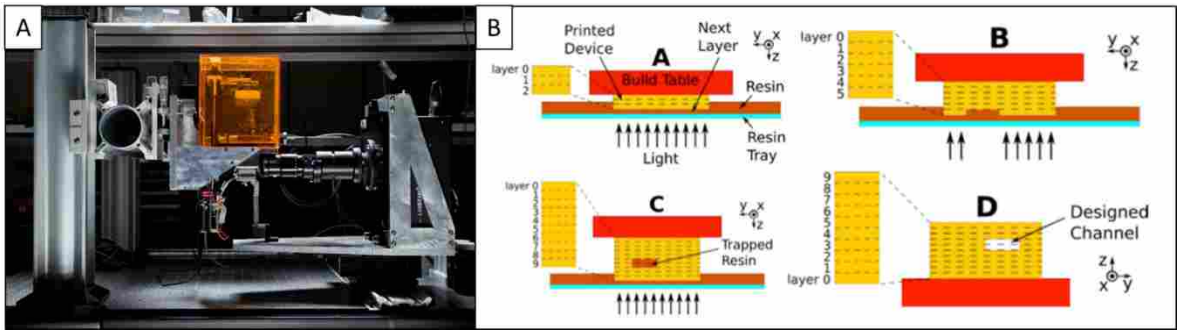

Figure 2.1 Stereolithographic 3D printing. *(A) Picture of the custom stereolithographic 3D printer.[2] (B) Schematic of how the custom stereolithographic 3D printer works (reprinted with permission).*[3]

pixel size of 7.6 μm. The build area of the printer is 19 mm × 12 mm. The build layer height was 10 μm and the normal exposure was 700 ms per layer. After the microfluidic devices were printed, excess resin was washed out with IPA, and the channels were vacuumed dry. Then, the devices were placed under an 11 mW 430 nm UV LED light (ThorLabs, Newton, NJ) for ~20 minutes for post curing.

2.2.1 Glass Slide Preparation

Glass microscope slides (3 in × 1 in × 1 mm) were scored using a laser cutter (Universal Laser Systems, Scottsdale, AZ). The settings on the laser cutter were 50% power, 10% speed, and 165 points per inch. The glass slides were then cleaned with acetone and IPA, and dried. The glass treatment solution was prepared by making a 10% by volume solution of 3-(trimethoxysilyl)propyl methacrylate in toluene. The glass slides were functionalized in this solution for 2 hours, after which they were taken out, washed with IPA, and dried. Then, the

glass slides were broken to the appropriate size for the 3D printer along the scored marks. The silianized glass slides were stored in toluene until they were used.

2.2.2 Resin Preparation

The 3D printing resin was prepared by making a solution of 2% NPS and 1% Irgacure 819 in 97% PEGDA. The solution was sonicated for 1 hour or until no solid particles remained in the solution. The resin was stored in an amber bottle wrapped in foil to prevent premature light exposure.

2.2.3 Description of 3D Printing Designs

The 3D print designs were made using the open source CAD software, OpenSCAD (openscad.org). The SCAD designs for the devices used can be seen in Figure 2.2. Both

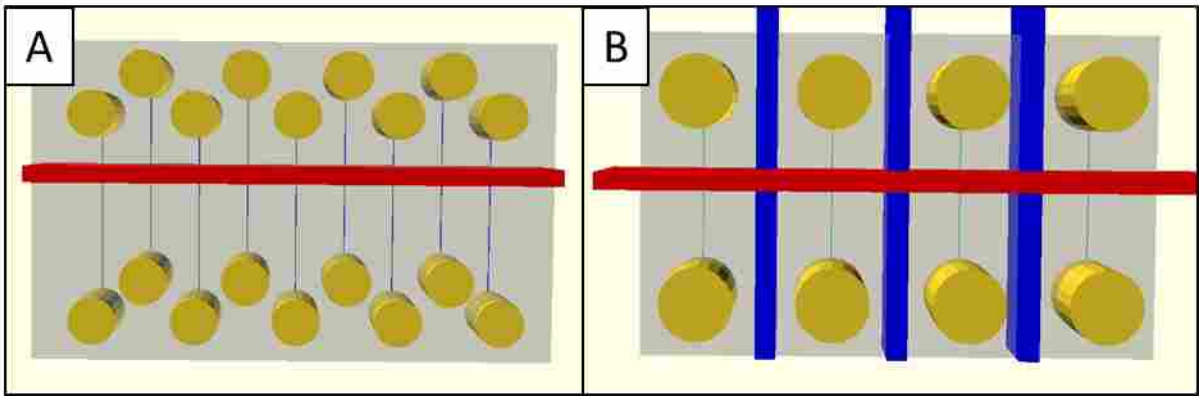

Figure 2.2 Image of SCAD designs for 3D printed microfluidic devices. *(A) Initial design. Yellow – reservoirs; blue – channels; red – monolith polymerization window. (B) Improved design. Yellow – reservoirs; light blue – channels; red – monolith polymerization window; blue – device divisions.*

designs are 12 mm wide and 19 mm long. They both contain straight channels that are 5 layers high by 6 pixels wide (50 μm x 45 μm) and have a reservoir on each end. This channel size was chosen to ensure that the smallest channels were printed that could remain uniformly open.

There is also a monolith polymerization window that is 600 μm wide and 6 layers above the channel that spans the length of both devices. The initial design has reservoirs that are 1 mm in diameter and 9 channels that are 6 mm long; the improved design has reservoirs that are 2.7 mm in diameter and only 4 channels that are 4.9 mm long. The initial design is 3.5 mm tall, whereas the improved design is 1.6 mm tall. The improved design also contains device divisions to separate each channel into an individual device.

2.2.4 Edge Compensation

An edge compensation technique was used to ensure that the channels were 45 μm wide.[45] This technique works by exposing 3 pixels adjacent to the channel and 4 layers above with two different exposures in a given layer. The first is a 400 ms exposure everywhere except at the 3 pixels adjacent to the channel, 4 layers above, and the channel itself. The second is a 330 ms exposure everywhere except in the channel itself. These two exposures help the channels to remain open but lessen light scattering and undesired polymerization in the channels, allowing for narrow channels to be successfully printed.

2.2.5 Water Contact Angle

The water contact angle was measured for the 3D printed material and compared to glass, PMMA, and COC. A device of about half the print area and 15 layers high was printed to test the 3D printed material. The 3D printed material, glass, PMMA, and COC were placed in 1 M HCl, 1 M NaOH, and water for 5 minutes, and then taken out and dried. A drop of water was placed on the surface and a photograph was taken. The image was then analyzed using ImageJ with the plugin drop analysis (NIH) to determine the water contact angle.

2.2.6 Device Stability

The stability of the devices was tested by printing a design that had 12 small test blocks as seen in Figure 2.3. The blocks contained 3 channels, 6 layers high, and 5 pixels wide (60 μm

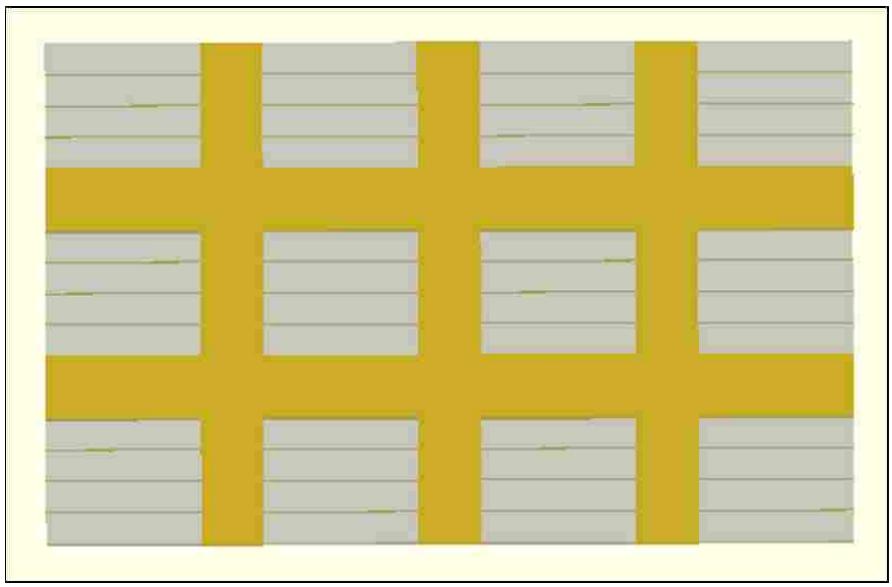

Figure 2.3 Image of SCAD design for test blocks with channels.

× 38 μm) that spanned the length of the block. The edge exposure on one print was 3 pixels around the channel and 4 layers above the channel for the entire device. The edge exposure on the other print was 3 pixels around the channel and 4 layers only directly above the channel. The printed blocks were submerged in water for 3 days. The stability of the blocks was analyzed using an ESEM XL30 (FEI, Thermo Fisher, Fair Lawn, NJ).

Other test blocks were printed without channels and then the layer exposure was varied through the height of the block. The exposure times for the different layers are listed in Table 2.1. These blocks were then post exposed for 5 minutes or 20 minutes under the LED source

Table 2.1: Exposure Times for Each Layer in Test Block

Layer	Exposure Time (ms)
0-40	1500
41-60	700
61-80	500
81-100	700
101-130	400/300
131-160	700
161-190	400/230
191-220	700
220-300	1500

described in section 2.2 and then submerged in water for 1 day. The stability of the blocks was analyzed using a Zeta 20 optical profilometer (Zeta, San Jose, CA).

2.3 Monolith Preparation

A GMA-EGDMA monolith was polymerized in the microfluidic channels within 3D printed devices. The monolith 1 mixture was prepared using 20% GMA (monomer), 10% EGDMA (crosslinker), 25% cyclohexanol (porogen), 25% 1-dodecanol (porogen), and 20% Tween 20 (surfactant). The monolith 2 mixture was prepared using 24% GMA (monomer), 11% EGDMA (crosslinker), 10% cyclohexanol (porogen) and 55% 1-dodecanol (porogen). These solutions were sonicated for 10 minutes. Then 1% DMPA (photoinitiator) was added and the mixtures were sonicated for 10 more minutes. The sonicated solution with the photoinitiator was then added to the channels which filled by capillary action. The reservoirs were then covered with tape, PDMS, or a 3D printed cap to prevent evaporation and polymerization within the reservoirs. The device containing the monolith solution was then placed under a SunRay 600 UV lamp for 10 minutes of UV exposure at 25.4 mW. After UV exposure, the unpolymerized

resin was removed from the monolith by flushing the channel with IPA for 30 minutes. Then, the monolith was emptied using a vacuum and stored dry until use.

2.3.1 SEM

The monoliths were imaged using scanning electron microscopy (SEM). To prepare for imaging, the 3D printed devices were removed from the glass slide using a razor blade and the monolith was cut through to be imaged. These pieces were placed on aluminum stubs and attached using carbon tape. The pieces were then coated with ~16 nm Au-Pd coating to reduce the charging during imaging. The images were taken using an ESEM XL30 in high vacuum mode at 10 kV electron beam potential. The nodule and pore sizes were analyzed using ImageJ from the generated SEM images.

2.4 Antibody Characterization and Immobilization

The compatibility of antiferritin and antilactoferrin with their respective antigens was evaluated using a dot blot test. First 1 μg/mL solutions of ferritin and lactoferrin were prepared in 20 mM phosphate buffer pH 7. Then, 2 μL of the ferritin and lactoferrin solutions were dotted on nitrocellulose paper (Bio-Rad, Hercules, CA) and left to dry for 30 minutes. Next, the remaining exposed part of the nitrocellulose paper was blocked for one hour with a solution of 5% dry milk in Tris buffer saline Tween buffer (TBST). After blocking, the nitrocellulose papers were washed 3 times with TBST for 5 minutes each. The papers were then incubated in their respective antibody (1 μg/mL in TBST) for 1 hour. After incubation, the papers were rinsed 3 times in TBST for 5 minutes each. Finally, the papers were incubated with a secondary fluorescent antibody at a concentration of 1 μg/mL in TBST for 1 hour. After 1 hour, the papers

were washed with TBST twice for 5 minutes each followed by a 10 minute rinse with Tris buffer saline (TBS). The papers were imaged on an Odyssey CLx scanner (Li-Cor, Lincoln, NE) to see if the antibody bound to its respective antigen.

Antibodies were immobilized on the GMA monolith with the reactive epoxy groups. About 5 μL of antibody solution (2 mg/mL) was added to one reservoir and allowed to flow through the monolith by capillary action. After the entire channel was filled, the excess antibody solution was removed from the reservoirs and they were refilled with 20 mM borate buffer (pH 8.5) and left to immobilize overnight. After this immobilization time, the channel was filled with 0.1 M Tris buffer (pH 8.5) and left for 1 hour to block the remaining reactive sites on the monolith. After blocking, the monoliths were washed thoroughly with 20 mM phosphate buffer pH 7 to remove the excess Tris buffer. For control experiments no antibody was added but the monolith was still blocked with Tris buffer.

2.5 Sample Preparation

The PTB biomarkers, ferritin, lactoferrin and CRF, and their antibodies were fluorescently labeled by dissolving them in 10 mM bicarbonate buffer (pH 10, BCB). Alexa Fluor 532 was dissolved in DMSO to a concentration of 1.4 mM. Enough Alexa Fluor 532 was added to the PTB biomarker solution so that the ratio of dye-to-ferritin and lactoferrin was 30:1, the ratio of dye-to-CRF was 1.5:1, and the ratio of the dye-to-antibody was 10:1. The solutions were incubated overnight in the dark at room temperature. Afterward the solutions were filtered four times for 15 minutes at 1400 RPM with a 30 kDa filter for the ferritin and lactoferrin and a 10 kDa filter for the antibodies to remove excess dye. CRF was not filtered due to its small size. Finally the labeled biomarkers were diluted in 20 mM phosphate (pH 7) to the desired

concentration before use. The antibodies were diluted in 20 mM borate buffer (pH 8.5) before use.

For labeling human serum, 10 µL of serum was mixed with 90 µL of 10 mM bicarbonate buffer (pH 10, BCB). Then 60 µL of Alexa Fluor 532 (1.4 mM) was added to the diluted serum and left overnight in the dark at room temperature to incubate. Afterward the solution was filtered four times for 15 minutes at 1400 RPM using a 3 kDa filter to remove excess dye. A 5000-fold diluted sample was then made in 10 mM bicarbonate buffer (pH 10, BCB). A spiked serum sample was made by taking 50 µL of labeled ferritin (100 nM), 20 µL of labeled serum (1000x diluted), and 30 µL of buffer so that the resulting concentration of ferritin was 50 nM and the resulting dilution factor of the serum was 5000.

2.6 Experimental Setup

A laser induced fluorescence (LIF) detection system used a 532 nm laser (Laserglow Technologies, Toronto, ON) directed into a Zeiss Axio Observer A1 inverted microscope (Jena, Germany) with a Chroma ET-532 nm laser bandpass filter set (Rockingham, VT). The laser light passed through a 20× objective at the desired detection point below the monolith. As the labeled analytes passed the detection point they produced a fluorescence signal that was detected by a Hamamatsu PMT (Bridgewater, NJ) connected to a Stanford Research Systems SR-560 preamplifier (Sunnyvale, CA). The analog PMT signal was digitized and amplified by a NI USB-6212 analog-to-digital converter (National Instruments) and recorded at 20 Hz using LabVIEW software (National Instruments). Platinum electrodes were used to apply the desired voltages to the channels. These voltages were controlled using a high voltage power supply (Stanford Research Systems).

For vacuum and fluorescent antibody experiments, images were taken using a Photometrics coolSNAP HQ2 CCD camera (Tucson, AZ) and a 4x objective. The images were taken with exposure times between 100- 400 ms and the images were analyzed using ImageJ software.

2.7 Device Operation

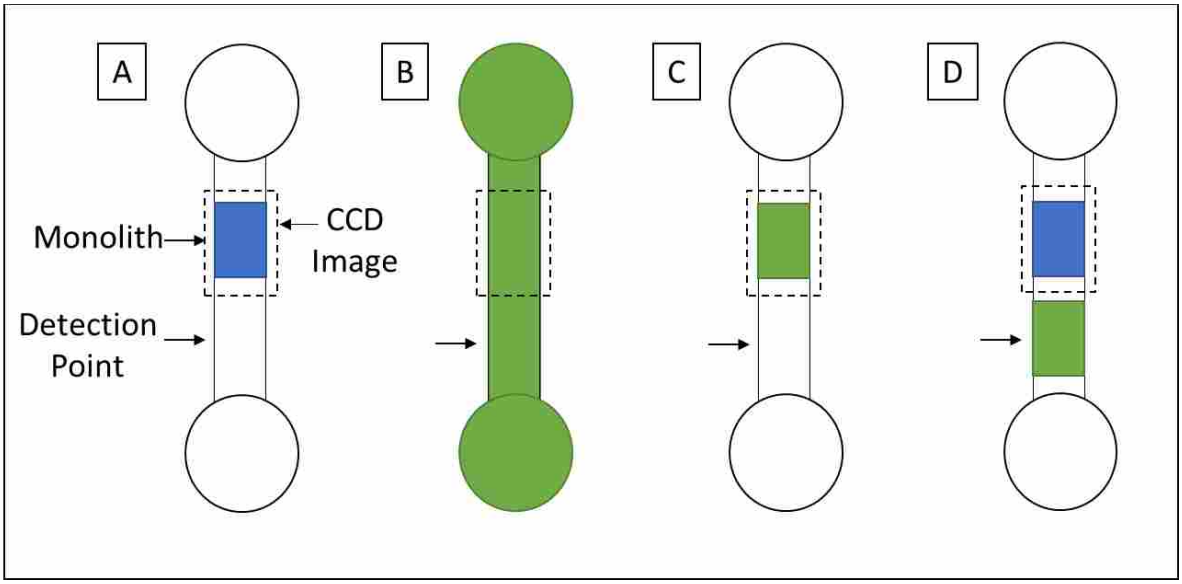

Figure 2.4 Device operation schematic. *(A) Blank step, (B) load step, (C) rinse step, and (D) elution step. A voltage or vacuum is applied to the channel to move the solutions.*

A schematic of the device operation can be seen in Figure 2.4. For voltage experiments, the channels were first filled with 20 mM phosphate buffer (pH 7). The channels were rinsed until there were no bubbles present. Then, +100 V was applied for one minute to equilibrate the channel. Next the reservoirs were emptied; labeled sample was added to the top reservoir and the bottom reservoir was refilled with fresh buffer. The voltage was applied for 2 minutes to load the sample through the channel. Next, the voltage was turned off and the channel was left for 10 minutes to incubate the labeled PTB analyte with the antibody on the monolith. Then, excess sample in the reservoir was removed and the top reservoir was washed with buffer 3 times. Both

reservoirs were emptied and filled with rinsing buffer (20 mM phosphate, pH 7). The voltage was reapplied for 2 minutes for rinsing. This process was repeated 3 times until the entire channel was rinsed out (except for any analyte bound to the antibody on the monolith) and the signal had returned to baseline. Then, the rinsing buffer was removed from the top reservoir and elution buffer (50 mM BCB, pH 10) was added. The bottom reservoir was also emptied and filled with fresh buffer. Finally the voltage was applied and the elution peak was recorded as the eluted sample passed the detection point.

For vacuum experiments, a vacuum was applied for a given amount of time for each step instead of applying a voltage. Volumetric flow rates were approximately 1.5 µL/min. Vacuum was applied for 1 minute in the load step, 5 minutes for the first rinse, another 5 minutes for the second rinse, and 2 minutes for the elution. CCD images were taken after each step.

2.8 References

1. Gong, H.; Bickham, B. P.; Woolley, A. T.; Nordin, G. P., Custom 3D printer and resin for 18 µm x 20 µm microfluidic flow channels. *Lab Chip* **2017,** *17* (17), 2899-2909.

2. Hollingshead, T. Professors 3D-print first truly microfluidic "lab on a chip" device. https://news.byu.edu/news/professors-3d-print-first-truly-microfluidic-lab-chip-device.

3. Gong, H.; Beauchamp, M.; Perry, S.; Woolley, A. T.; Nordin, G. P., Optical approach to resin formulation for 3D printed microfluidics. *RSC Adv.* **2015,** *5* (129), 106621-106632.

3. RESULTS AND DISCUSSION

3.1 3D Printed Device Properties

Because these are the first chemical analysis experiments with this 3D printed material, some properties of the 3D printed material were tested.

3.1.1 Water Contact Angle

First, the water contact angle of the 3D printed material was measured before and after exposure to 1M HCl and 1M NaOH to see if the surface changed with exposure to different pHs. These water contact angle measurements were compared to those for other materials commonly used for making microfluidic devices under the same conditions. The results can be seen in Figure 3.1. The water contact angle for the 3D print increased 9 degrees when exposed to 1 M

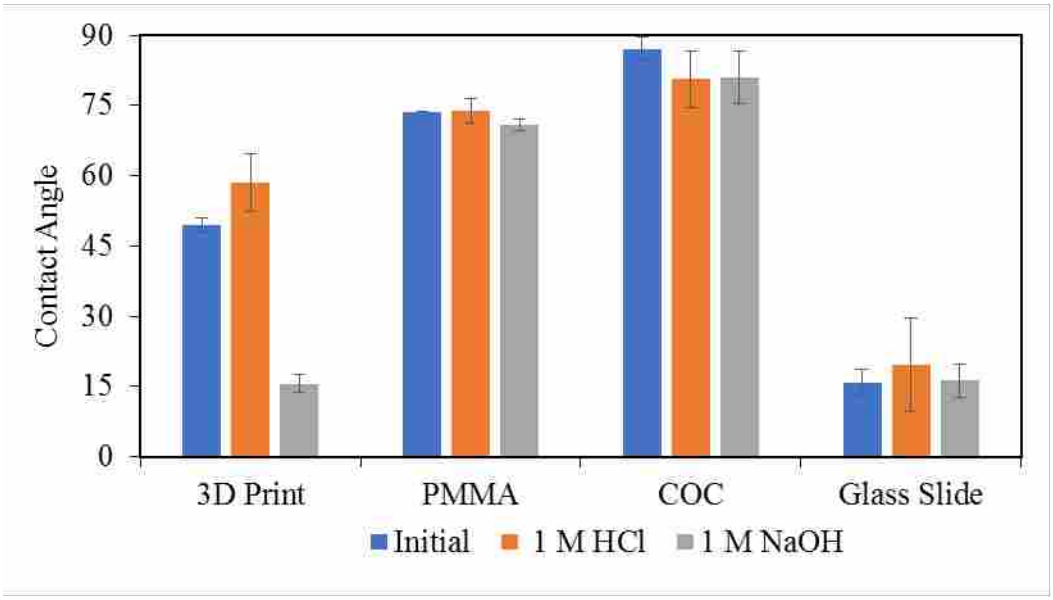

Figure 3.1 Water contact angles of 3D printed material, PMMA, COC, and a glass slide before and after being exposed to 1 M HCl and 1 M NaOH. *Error bars show ± 1 standard deviation (for Initial n = 3, for 1 M HCl and 1 M NaOH n = 6).*

HCl and decreased 34 degrees when exposed to 1 M NaOH. For PMMA, COC, and the glass slide the greatest change for the water contact angle before or after being exposed to 1 M NaOH or 1 M HCl was less than 6 degrees. Thus, compared to the other materials, the 3D printed material surface is more susceptible to changes in environment and especially after contact with a strong base. This may be because the 3D printed material has many ester groups that can be hydrolyzed when exposed to strong base, thus increasing the polarity and hydrophilicity of the surface.

3.1.2 Edge Compensation

The stability of the microfluidic devices after being exposed to water and how this stability could be improved was also studied. Since the 3D printer is custom built, the movement of the 3D printer stage and the exposure times for each layer could completely be controlled. Thus, as described previously[1] and in Chapter 2.2.4, a technique called edge compensation can be used to improve the formation of small void features within 3D prints. For the edge compensation, the light exposure directly around the channel is decreased to limit unwanted polymerization into the channel and to ensure that the resin can be cleared from the channels. In this area surrounding the channel, the device is underexposed, so there is less polymerization, making the material less stable. Thus, by limiting areas where the device is underexposed, the stability of the device can be increased. Small test blocks with 3 channels each were made with different edge exposure compensation patterns as described in Chapter 2.2.6. The blocks were placed in water for 3 days to see if the block stability degraded over time. Then SEM images were taken to observe if the devices remained intact (stable) or had cracks indicating instability;

for example, see Figure 3.2. The blocks in Figures 3.2A-B had an edge compensation pattern where they were underexposed for the 4 layers above the channel across the entire device. The

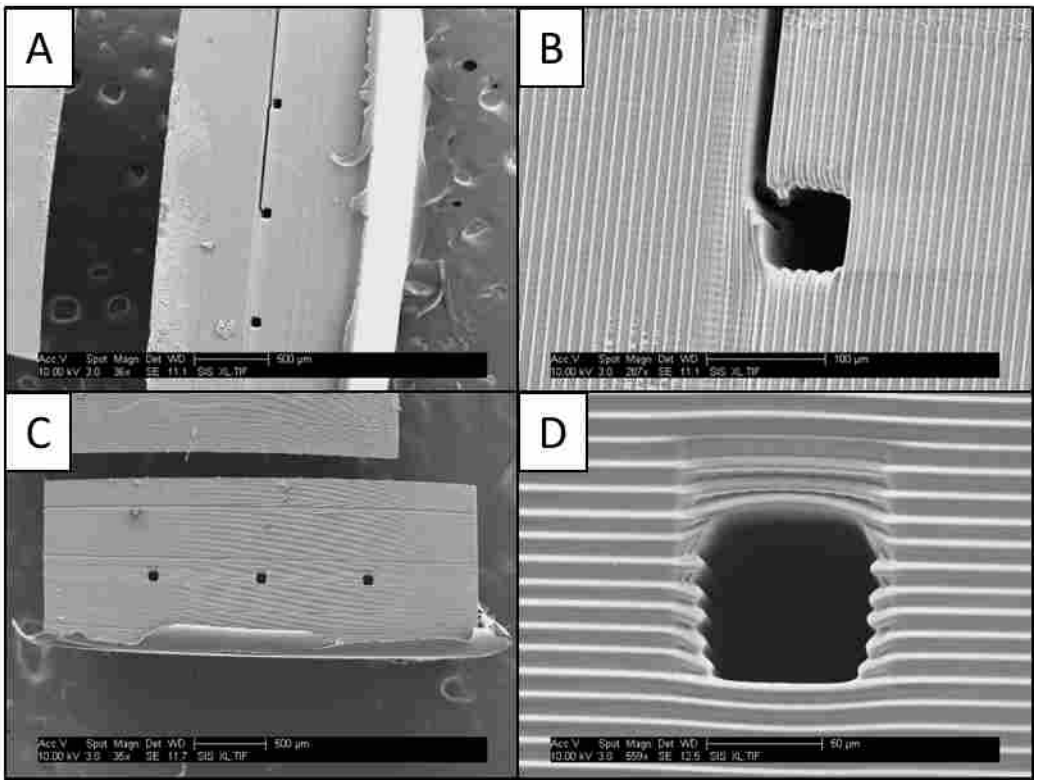

Figure 3.2 SEM images of test blocks with different edge exposure patterns*. (A) Underexposed for 4 layers above the channel across the whole device (top of the block is on the left). (B) Zoomed image of one channel in (A). (C) Underexposed for 4 layers only directly above the channel (top of the block is the top of the image). (D) Zoomed image of one channel in (C).*

underexposed layers can be seen as a lighter region in Figure 3.2A and as different sized layers in Figure 3.2B to the left side of the channels in the images. As can be seen, the blocks experienced cracking in the underexposed region. This cracking would often span the distance between two channels, connecting them. However, when underexposure was only directly above the channels, no cracking was observed near the channels (Figures 3.2C-D). Therefore, areas where there is less light exposure lead to weaknesses in the device which can be minimized if the lower exposure time is localized to a limited region.

3.1.3 Post Exposure

Post exposure time was also evaluated to improve device stability. As seen in the edge compensation experiments, cracks form between layers where a layer has a different exposure time from the layers next to it. Thus, test blocks were made as described in Chapter 2.2.6 and Table 2.1 and submerged in water for 1 day to see if the blocks' stability degraded over time. The extent of cracking (indicating instability) was analyzed using a profilometer and the results can be seen in Figure 3.3. The blocks that were exposed 5 minutes showed cracks as indicated

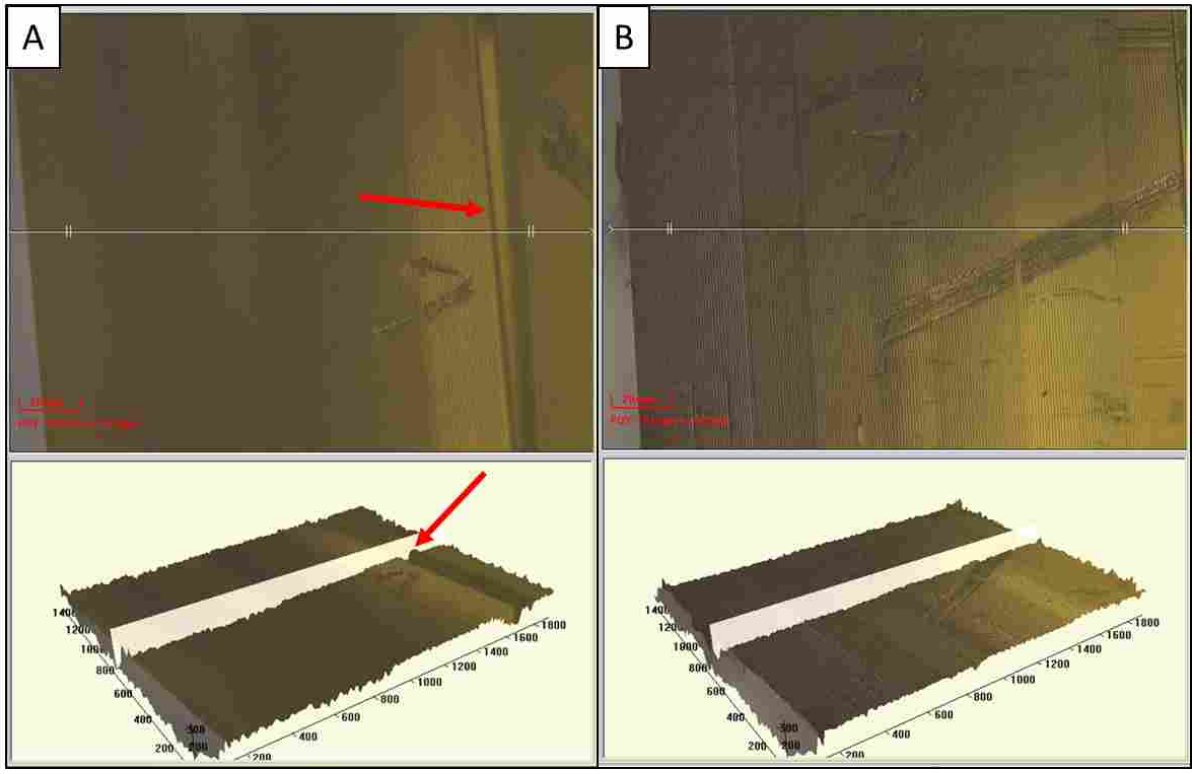

Figure 3.3 Side view images of block cracking taken with the profilometer. *(A) 5 minute post exposure. (B) 20 minute post exposure. Top of test block is on the right. Red arrows indicate places where the block is cracked.*

by a dip in the profilometer topography map. These cracks were between layers with dissimilar exposure times as expected. The blocks that were exposed for 20 minutes did not show cracking. Thus, the longer post exposure helped to prevent cracking, especially between layers with dissimilar exposure times.

3.2 Device Designs

3.2.1 Initial Device Design

A 3D printed microfluidic device was designed and printed as described in Chapter 2.2. A photograph of a 3D printed microfluidic device can be seen in Figure 3.4. In this initial device

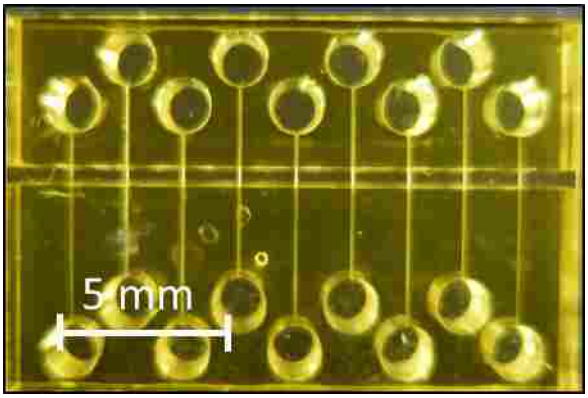

Figure 3.4. Photograph of the initial 3D printed microfluidic device design.

design there are nine channels to enable multiple experiments to be done on a single print. However, to maximize space on the device for these 9 channels, the reservoirs are only 1 mm in diameter. Thus, to ensure the reservoirs hold a sufficient volume of buffer for experiments, the device is 3.5 mm tall so that the total volume held by the reservoirs is about 4 μL.

The trench that runs the length of the device, or monolith polymerization window, was designed to allow for the polymerization of the monolith in the channel. This window was necessary because the device material contains NPS which is a UV absorber; thus, the device material does not allow for sufficient penetration of UV light necessary to form monoliths. By having less material above the channel in the area where the monolith will be polymerized, the UV light can more easily penetrate that area and polymerize the monolith. The device itself thus acts as a mask to shield the part of the channel where I do not want the monolith to form. By adjusting the monolith polymerization window I can change the size and location of the monolith

in the channel. It was determined that 6 layers (60 μm) above the channel would still allow polymerization of the monolith and that 600 μm was a sufficient length for the monolith.

This initial 3D printed device design was used to perform many experiments. However, as more experiments were performed it became apparent that there were flaws in the design. Frequently, cracks formed in the devices as seen in Figure 3.5. These cracks connected

Figure 3.5 Side view of monolith window cracking taken with the profilometer. *Red arrow indicates a place where the device is cracked.*

channels, changing the flow profile and current in the channel. In addition, something fluorescent was observed in some of the channels before any fluorescent sample had been added. It was hypothesized that the fluorescence in the channels was caused by channels connecting through cracks formed between them. For these reasons it was difficult to get consistent results with the initial design. However because of 3D printing's rapid design to fabrication nature, I was quickly able to make an improved design taking into account the problems with my original device and the things learned in the stability experiments from sections 3.1.2 and 3.1.3.

3.2.2 Improved Device Design

A photograph of the improved device design for immunoaffinity extraction experiments can be seen in Figure 3.6. The device is about half the height of the previous one to ensure that

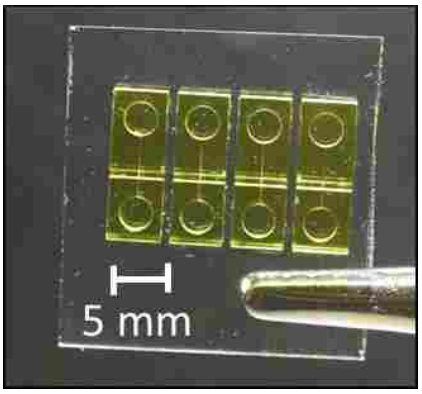

Figure 3.6 Photograph of the improved 3D printed microfluidic device design.

the post exposure penetrates through the entire device to increase the stability. There are 4 identical channels that are each separated by a 0.5 mm gap so that even if a crack forms through one channel it cannot spread to another channel and cause cross-talk. The reservoirs were also made larger (2.7 mm diameter) to increase the volume that they can hold to about 6 μL. The channel and monolith polymerization window parameters remained the same because they already were optimized for the printer and the monolith. With these changes in the device design, the prints turned out consistently and no cracking was observed.

3.3 Monoliths

3.3.1 Initial Monolith Formulation

Another graduate student previously developed an affinity monolith (monolith 1)[2], as described in Chapter 2.3. Using this formulation monoliths were successfully formed in 3D printed microfluidic devices. A variety of exposure times were tested, and it was ultimately determined that an exposure time of 10 minutes produced the most consistent, well polymerized monoliths that allowed sufficient flow for experiments. SEM images of the monolith can be seen in Figure 3.7. These SEM images show that the monolith is well attached to all sides of the

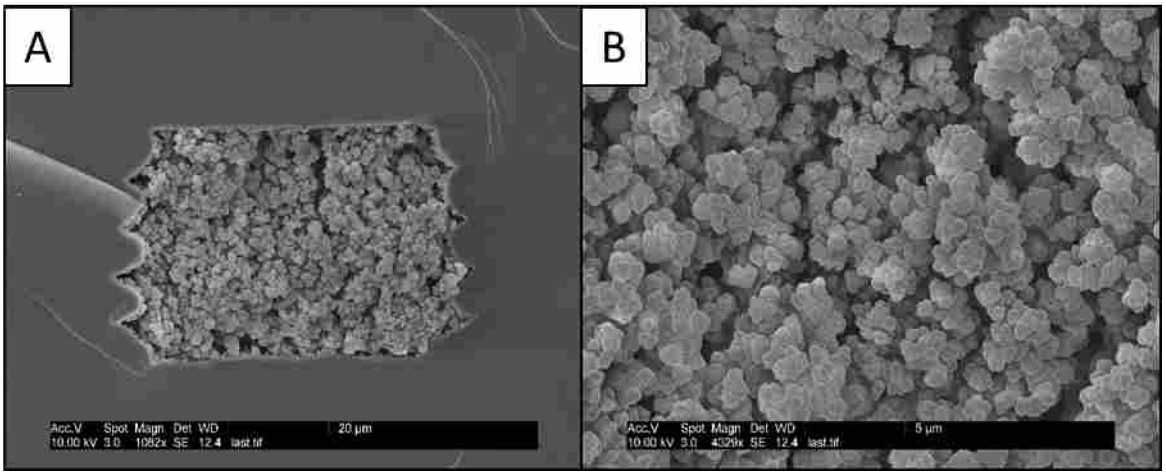

Figure 3.7. SEM images of monoliths formed in the initial device design with 10 minute exposure. *(A) Whole channel view. (B) Zoom view.*

channel. The average nodule size was 0.95 μm and the average pore size was 2.11 μm. However, in this monolith formulation Tween 20, a surfactant, is added to aid with solubility but is not essential for formation of the monolith. In an effort to simplify the monolith composition, a new monolith formulation was developed that did not contain Tween 20.

3.3.2 Improved Monolith Formulation

Monoliths were formed from both the old (monolith 1) and new (monolith 2) formulas. To compare the two formulas, SEM images were taken of each monolith, as seen in Figure 3.8. When comparing Figure 3.8 B and D, monolith 2 has rougher looking nodules than

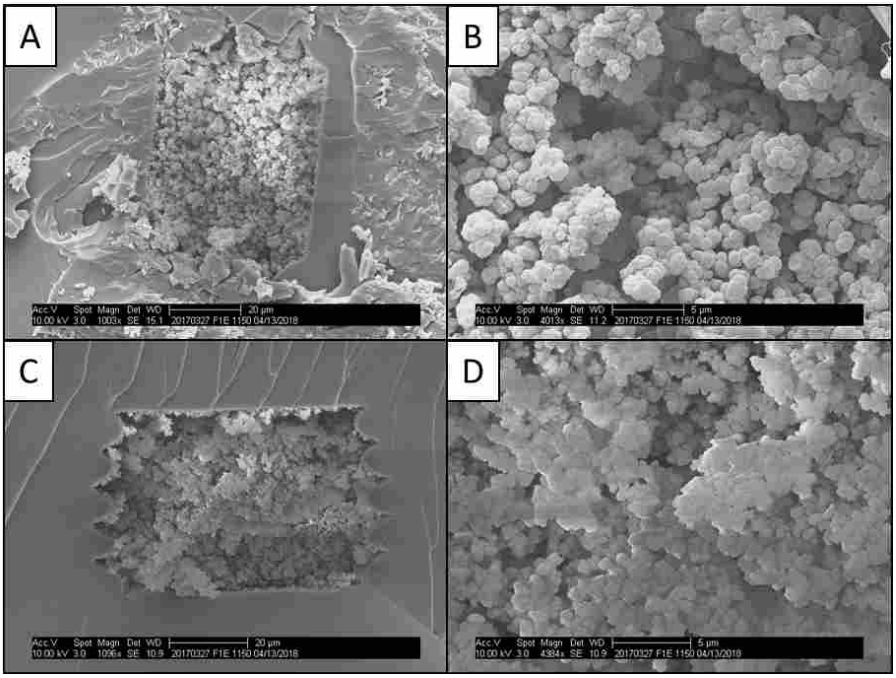

Figure 3.8 SEM images of monoliths 1 and 2 made in devices with the improved design. *(A) Monolith 1. (B) Zoomed in monolith 1. (C) Monolith 2. (D) Zoomed in monolith 2.*

the nodules in monolith 1. However, when comparing the pore and nodule sizes they were similar for both formulas. The average pore size for monolith 1 was 2 μm (std. = ± 0.7, n = 7) and the average nodule size was 1 μm (std. = ± 0.1, n = 3). The average pore size for monolith 2 was 2 μm (std. = ± 1, n = 7) and the average nodule size was 0.7 μm (std. = ± 0.05, n = 3). The SEM images also show that both monoliths have good attachment to the walls. Thus, both monoliths were used until it was determined by experiment which monolith performed better.

3.4 Antibodies

3.4.1 Attachment of Antibody to Monolith

The attachment of antibody onto two different monoliths was verified by CCD imaging before and after immobilization of labeled antiferritin. The CCD images and resulting

background-subtracted fluorescence measurements of the monoliths with labeled antibody can be seen in Figure 3.9. Monolith 2 formulation (without Tween 20) has more antibody attachment

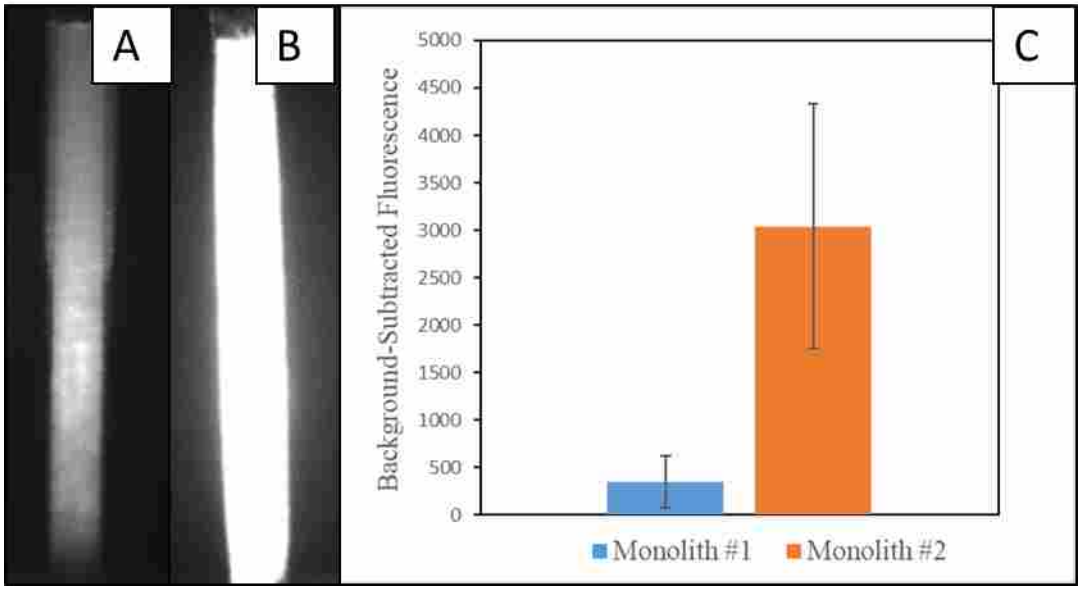

Figure 3.9 Labeled antibody attachment. *(A) CCD image of monolith 1 with labeled antibody attached. (B) CCD image of monolith 2 with labeled antibody attached. (C) Background-subtracted fluorescence of monolith 1 and monolith 2 after immobilization of labeled antiferritin. Error bars indicate ± 1 standard deviation and n = 3. These experiments were performed in devices with the improved design.*

than monolith 1 which contains Tween 20. It appears that Tween 20 interferes with the attachment of antibody to the monolith. In subsequent experiments monolith 2 (no Tween 20) was used.

3.4.2 Dot Blots

A dot blot was performed to verify that the ferritin and antiferritin samples, and lactoferrin and antilactoferrin samples were compatible. A fluorescence image of the dot blots can be seen in Figure 3.10. As indicated by the presence of two fluorescent dots in each panel,

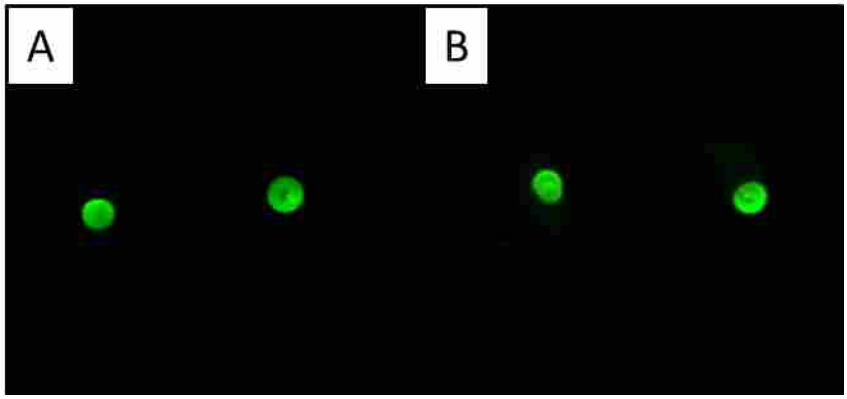

Figure1 3.10 Dot blots of (A) ferritin and antiferritin and (B) lactoferrin and antilactoferrin.

ferritin and antiferritin are compatible as an antigen-antibody pair, and so are lactoferrin and antilactoferrin.

3.5 Establishing Experimental Conditions

Once the 3D printed microfluidic device was designed and printed with a monolith formed, other conditions were tested in order to perform immunoaffinity extraction of PTB biomarkers.

3.5.1 Rinsing Buffer

First, the rinsing buffer composition was considered. Solutions of 1 μM Alexa Fluor 532 in phosphate and HEPES were compared and analyzed on the Nanodrop. The average fluorescence for Alexa Fluor 532 in HEPES and phosphate as a function of wavelength can be seen in Figure 3.11. Alexa Fluor 532 was 12 times more fluorescent in phosphate than HEPES.

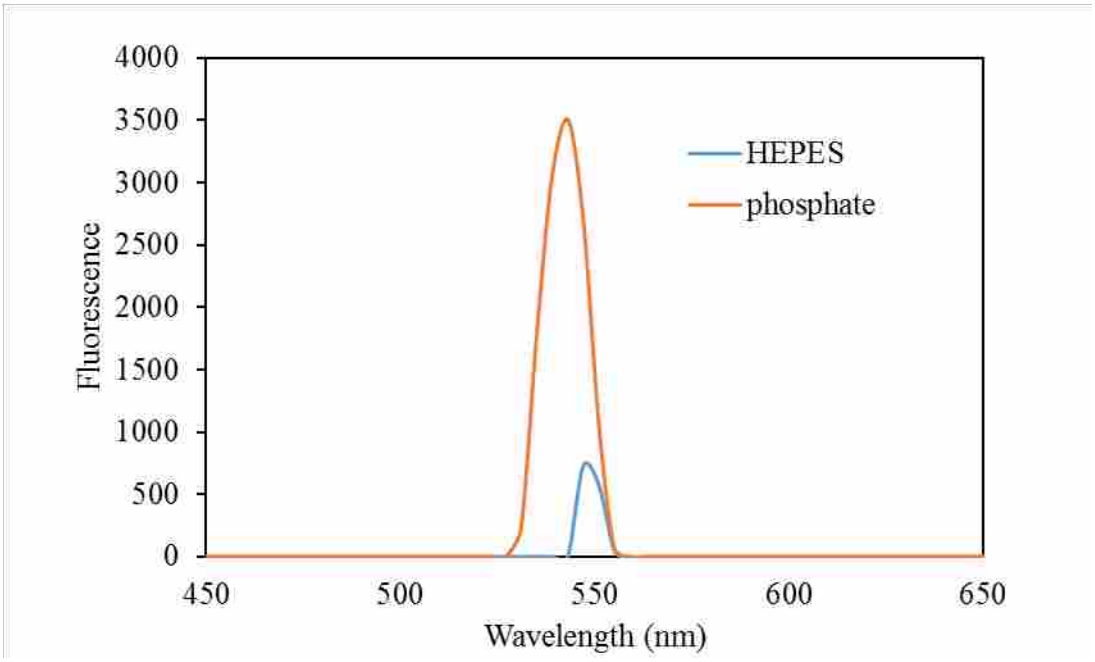

Figure 3.11. Fluorescent spectra of 1 µM Alexa Fluor 532 in 20 mM phosphate pH 7 and 20 mM HEPES pH 7 (n = 3).

Thus, phosphate was used for the rinse in subsequent experiments to ensure that the maximum fluorescence was observed.

3.5.2 Voltage

Another parameter that was optimized was the voltage applied to the channel. Channels were filled with 20 mM phosphate buffer pH 7, a constant voltage was applied to the channel, and the current was recorded every 10 seconds. As can be seen in Figure 3.12, irregular

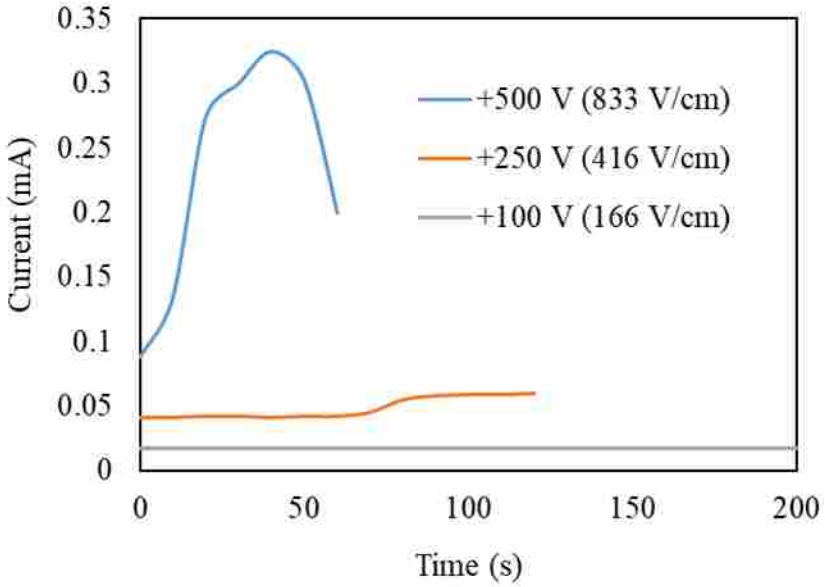

Figure 3.12. Comparison of observed current as a function of an applied voltage over time. *Done with the initial device design.*

current resulted at higher applied voltages. For +500 V the current changed dramatically over the course of a minute, increasing then dropping off quickly. However, for +100 V, the current remained constant for over 3 minutes. These irregularities in the current could be because the reservoirs only hold 4 µL of buffer so at higher applied voltages the ions are depleted more quickly. They could also be caused by Joule heating or bubbles forming due to electrolysis. Thus, +100 V was chosen as the applied voltage so that the current remained consistent the entire time it was being applied.

3.5.3 Vacuum vs Voltage

CCD imaging was used to look at sample loading onto the monolith with vacuum and with voltage as seen Figure 3.13. After applying +100 V to the channel for 2 minutes, the 50 nM

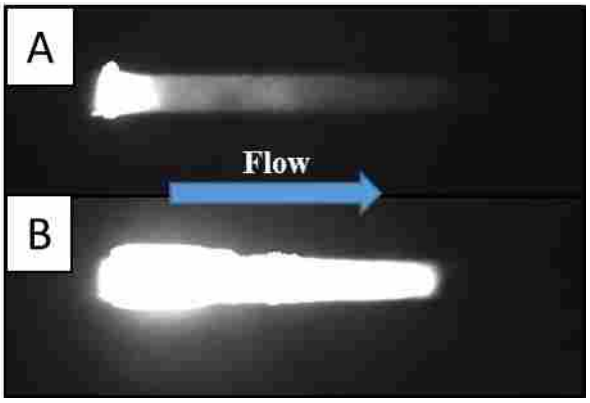

Figure 3.13. CCD images of sample loading with (A) voltage and (B) vacuum. *Experiments done in devices with the improved design.*

ferritin sample enters the monolith but does not flow much past the entrance of the monolith as seen in Figure 3.13A. After vacuum is applied on the same channel for 30 seconds, the sample moves through the entire monolith as seen in Figure 3.13B. Thus, using voltage to induce flow of the sample through the monolith is not as effective as using vacuum to pull the sample through. This may be due to the surface charges of the device relative to the surface charges on the monolith. For sample to move through the channel with applied voltage, the electrophoretic velocity of the analyte must exceed the electroosmotic velocity induced by the surface charges and voltage. Thus, a difference in electroosmotic flow in the monolith may hinder flow of sample through the monolith by voltage. Based on this result, all further experiments were done using vacuum to draw fluids through the monolith.

3.6 Extraction Experiments

3.6.1 Extraction of Lactoferrin

Voltage was used to move analyte and buffer through the channel and perform extraction in devices with the initial (9 channel) design. The conditions for this extraction were +100 V and

phosphate buffer pH 7, as determined by a previous graduate student[46] and outlined in Chapter 2.7. Labeled lactoferrin was first loaded through the channel. After an incubation period, the lactoferrin not attached to antibody was rinsed from the monolith. Finally, the lactoferrin attached to antibody was eluted and the fluorescence of the eluted ferritin was recorded as it passed the detection point. A high concentration of lactoferrin was required because the laser used in this study was failing and had low power. As can be seen in Figure 3.14, there is a peak around 60 seconds only for the antilactoferrin column, showing that lactoferrin was extracted.

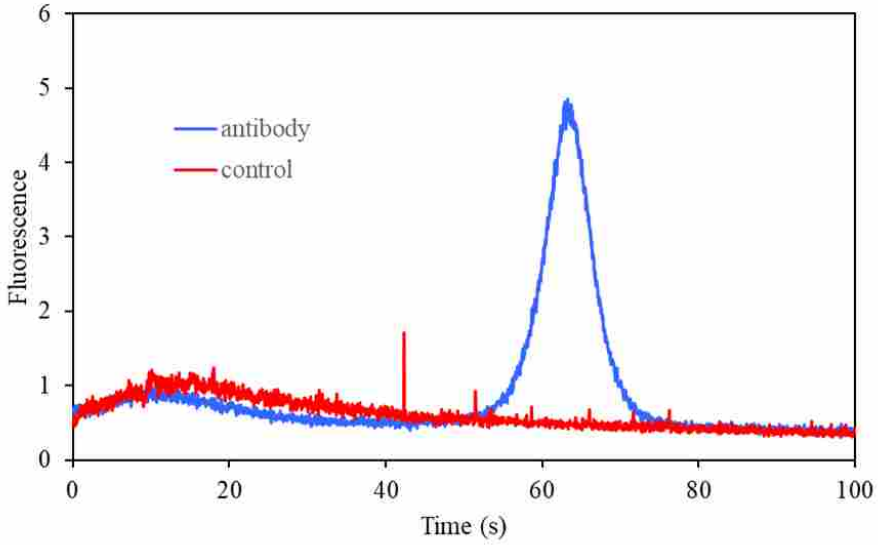

Figure 3.14 Elution after extraction of 5 µM lactoferrin on an unmodified monolith (control) and a monolith modified with anti-lactoferrin (antibody) in the initial (9 channel) device design.

Although this extraction was successful, it was difficult to repeat because of the problems observed with the initial device design such as cracking within the device that caused devices to break down and channels to connect. All further experiments were done on devices with the improved (4 channel) design.

3.6.2 Extraction of Ferritin

With the improved device design and using a vacuum to move fluids through the channel, ferritin was extracted on and eluted from a monolith with and without antiferritin. CCD images of the fluorescence on the monolith were taken after the loading, rinse 1, rinse 2, and elution steps as described in Chapter 2.7. The background-subtracted fluorescence on the monolith was determined at each step from CCD images (examples in Appendix 1.4), and the results can be seen in Figure 3.15. When antiferritin is attached to the monolith there is a smaller decrease in

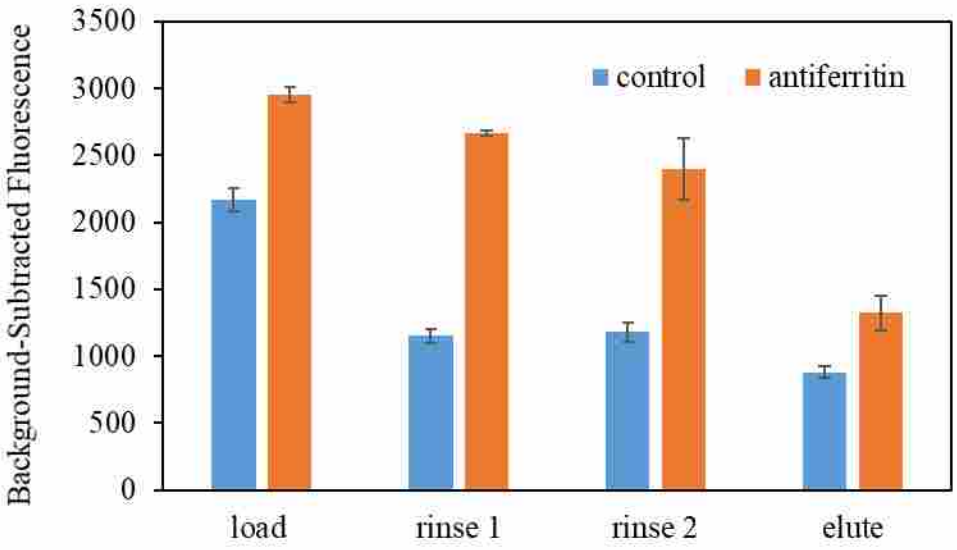

Figure 3.15 Immunoaffinity extraction of ferritin on both unmodified (control) and antiferritin modified monoliths. *Data from 2 replicate experiments. Error bars indicate ± 1 standard deviation.*

fluorescent signal from loading to the rinsing step than in the control, because the labeled ferritin that is attached to the antibody does not wash off in the rinsing step. For the control, rinse 1 and rinse 2 have similar background-subtracted fluorescence of around 1100 and after elution it drops 25% to around 900. This as expected because the majority of the labeled ferritin should rinse out in the initial rinse step since there is no antibody for the ferritin to attach to. The background-subtracted fluorescence is not zero because ferritin is also nonspecifically bound to

the monolith. By changing the rinse conditions, this nonspecific binding could be reduced in further studies. In the antibody experiment there is a much larger drop (almost 2 fold) in background-subtracted fluorescence from rinse 2 to elution. This indicates that much of the labeled ferritin that was retained by the antibody after the rinse step is no longer retained after the elution step. The larger drop in background-subtracted fluorescence with antibody attached to the monolith compared to the control indicates that ferritin was successfully extracted and eluted.

3.6.3 Confirmation of Ferritin Selectivity

To test the selectivity of antiferritin for ferritin, another PTB biomarker (CRF) was flowed through a monolith with attached antiferritin. The same conditions were used for 1 µM CRF as were used for the extraction of ferritin (example CCD images are Appendix 1.4). As shown in Figure 3.16, CRF flowed through the monolith, as indicated by the high

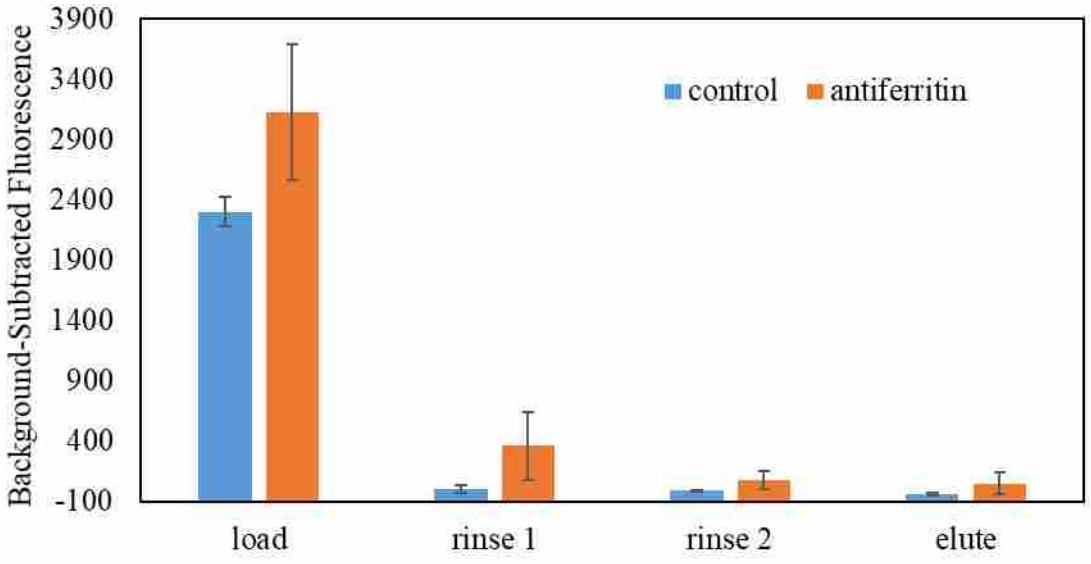

Figure 3.16. Extraction of 1 µM CRF on a monolith with (antiferritin) and without (control) antiferritin attached. *Data from 2 replicate experiments. Error bars show ± 1 standard deviation.*

background-subtracted fluorescence in the load step. However after rinse 1, the background-subtracted fluorescence dropped significantly indicating that labeled CRF was not retained and was rinsed out of the monolith. It followed that rinse 2 and the elution both had low background-subtracted fluorescence, like rinse 1, showing that CRF was rinsed out and not retained by antiferritin on the monolith. This same pattern is observed in the control where no antiferritin is present. These results confirm that CRF is not retained by antiferritin because CRF behaves the same with or without antiferritin present. Thus, the extraction of ferritin using antiferritin is selective to ferritin.

3.6.4 Extraction of Ferritin from a Human Blood Serum Sample

A serum sample spiked with ferritin was prepared as described in Chapter 2.4. This spiked serum sample was flowed through monoliths with or without antiferritin attached. The conditions were the same as used previously for the extraction of ferritin and as outlined in Chapter 2.7 (example CCD images are Appendix 1.4). As seen in Figure 3.17, for the

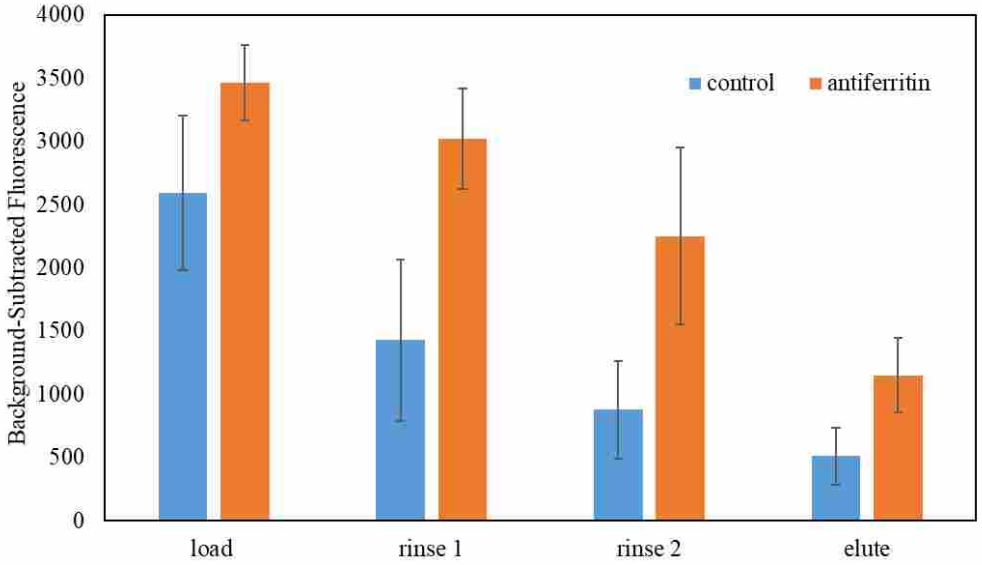

Figure 3.17 Extraction of spiked serum on a monolith with (antiferritin) and without (control) antiferritin attached. *Data from 4 replicate experiments. Error bars indicate ±1 standard deviation.*

control the largest drop in background-subtracted fluorescence is between the load and rinse 1 steps, a 45% decrease. In contrast, when antiferritin is attached, the drop in background-subtracted fluorescence between the load and rinse 1 steps is only 12%. This is because in the control there is no antibody to retain the ferritin, so most of the ferritin is rinsed out in the first step; whereas, when there is antiferritin, the ferritin is retained so much less is rinsed out in rinse 1. The largest drop in background-subtracted fluorescence when antiferritin is attached to the monolith is between rinse 2 and elution steps, a 60% decrease. The difference between rinse 2 and the elution steps for the control is smaller at 40%. This indicates that the ferritin that was retained by the antiferritin is eluted because the fluorescence signal drop is greater for the experiment with antiferritin than without. There is residual fluorescence after the elution step for both the control and the antiferritin experiments, as there was in the ferritin experiment, likely because some ferritin is nonspecifically bound to the monolith. This can be improved by changing the rinsing conditions for the experiment. The differences in column fluorescence between the experiments with antiferritin and without it give support to the assertion that ferritin was extracted from the spiked serum sample.

3.7 References

1. Gong, H.; Bickham, B. P.; Woolley, A. T.; Nordin, G. P., Custom 3D printer and resin for 18 mu m x 20 mu m microfluidic flow channels. *Lab Chip* **2017,** *17* (17), 2899-2909.

2. Sonker, M.; Parker, E. K.; Nielsen, A. V.; Sahore, V.; Woolley, A. T., Electrokinetically operated microfluidic devices for integrated immunoaffinity monolith extraction and electrophoretic separation of preterm birth biomarkers. *Analyst* **2018,** *143* (1), 224-231.

4. CONCLUSIONS AND FUTURE WORK

4.1 Conclusions

3D printing is a promising new method for the fabrication of microfluidic devices. It is quick, inexpensive, and convenient for making small 3D features. Furthermore, it allows for an iterative process where something can be designed on a computer, fabricated immediately, and then tested experimentally. An evaluation of how the component performs in experiments then guides further design improvements. In this thesis, I have shown that a 3D printed device for immunoaffinity extraction can be made and that the design can be improved when flaws are found during experimentation. The improved design does not crack, and this leads to more consistent results. In addition, I have presented that monoliths can be polymerized in these devices and have demonstrated that the device itself can be a mask for the specific polymerization of these monoliths in the desired location in the microfluidic channel. This work also shows that ferritin can be extracted selectively with antiferritin. Finally, this research shows that ferritin can be extracted from human blood serum samples in these 3D printed immunoaffinity devices.

4.2 Future Work

Based on the results from this work, more research can be done to optimize the extraction conditions. As can be seen in Figures 3.15 and 3.17, labeled ferritin is still attached to the monolith after rinsing and elution for both the control and antibody columns. It should be possible to rinse more thoroughly to remove the nonspecifically bound ferritin by changing the pH, concentration, or composition of rinsing buffer. In addition, it may be possible to recover

more of the extracted ferritin from the monolith by adding more salt to the elution buffer to increase the ionic strength, or increasing the pH of the elution buffer.

My work has only shown that ferritin can be specifically extracted from a blood sample. More work needs to be done to show that all nine PTB biomarkers can be specifically extracted from human blood serum. To extract all 9 biomarkers, conditions must be developed for which all of the biomarkers can be extracted together or in a few groups. Additionally, cross reactivity of the different antibodies will need to be addressed.

One of the biggest contributions of my work is showing that extraction of a PTB biomarker from serum in 3D printed devices is possible. However in order for this extraction to be integrated with the other aspects of a PTB risk test, the steps in this extraction need to be more automated. Our collaborators have shown that pumps and valves can be 3D printed for microfluidic channels.[1-2] A proposed design for integrating pumps and valves to automate immunoaffinity extraction is shown in Figure 4.1. By including pumps and valves in this design

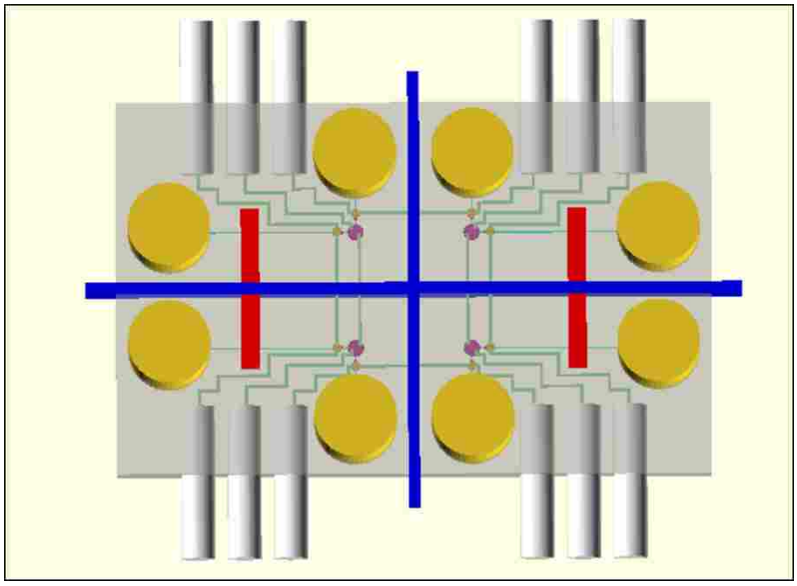

Figure 4.1 Proposed design for automated immunoaffinity extraction. *Yellow – reservoirs, light blue – fluidic channels, red – monolith polymerization window, blue – device divisions, green – pneumatic channels, white – pneumatic connection ports, orange and purple – pumps.*

we will be able to create a pressure-driven microfluidic system, which will be automated with consistent flow rates. Also with a pressure-driven system, the flow rates can be increased beyond those in the current devices so the extraction can be performed faster. Additionally, the automated pressure-driven system should allow for elution to be detected directly with a PMT. This work is a first step toward creating a 3D printed microfluidic PTB risk test. As 3D printed microfluidic devices for immunoaffinity extraction are improved, more applications should also be realized.

4.3 References

1. Gong, H.; Woolley, A. T.; Nordin, G. P., 3D printed high density, reversible, chip-to-chip microfluidic interconnects. *Lab Chip* **2018,** *18* (4), 639-647.

2. Gong, H.; Woolley, A. T.; Nordin, G. P., High density 3D printed microfluidic valves, pumps, and multiplexers. *Lab Chip* **2016,** *16* (13), 2450-2458.

Appendix 1

A 1.1 OpenSCAD Code for Initial Device Design

```
px = 0.0076;
layer = 0.010;
ReservoirRadius = 0.90;
compensation = false;    // set to true for compensation design

module bulk() {
    cube([2560*px,1600*px,350*layer]);
}

module channel_and_reservoirs(chanel_l, channel_w, channel_h) {
    // channel. true for compensation, false for normal
    if(!compensation)
        translate([-channel_w/2,0,layer]) color("cyan") cube([channel_w,
chanel_l+ReservoirRadius*2, channel_h]);
    else
        translate([-channel_w/2-3*px,0,layer]) color("yellow") cube([channel_w+6*px,
chanel_l+ReservoirRadius*2, channel_h+4*layer]);

    // reservoirs
    cylinder(3.5,ReservoirRadius,ReservoirRadius,$fn=20);
    translate([0, chanel_l+ReservoirRadius*2,0])
cylinder(3.5,ReservoirRadius,ReservoirRadius,$fn=20);
}

module all_channels() {
    for(i=[0:4]) translate([300*px+500*px*i, 200*px, 40*layer])
channel_and_reservoirs(800*px, 6*px, 5*layer);
    for(i=[0:3]) translate([550*px+500*px*i, 400*px, 40*layer])
channel_and_reservoirs(800*px, 6*px, 5*layer);
}

difference() {
    bulk();
    all_channels() ;

    // polymerization window 6 layer
    translate([-0.001,900*px,51*layer])color("purple")cube([2560*px+0.002,80*px,500*layer]);
}
```

A 1.2 OpenScad Code for Improved Device Design

```
pixel = 0.0076;
layer = 0.010;
ReservoirRadius = 1.35;
module bulk() {
   cube([2560*pixel,1600*pixel,150*layer]);
}

module featureX(break_l,break_w, break_h) {
  color("blue") cube([break_l,break_w,break_h]);
}
module featureY(chanel_l, channel_w, channel_h) {
   cylinder(3.5,ReservoirRadius,ReservoirRadius,$fn=20);
   translate([0,0,layer])
      color("cyan") cube([channel_w, chanel_l+ReservoirRadius*2, channel_h]);
   translate([0, chanel_l+ReservoirRadius*2,0])
      cylinder(3.5,ReservoirRadius,ReservoirRadius,$fn=20);
}
module all_channels() {
   for(i=[0:3]) {
      translate([300*pixel+650*pixel*i, 300*pixel, 40*layer])
         featureY(650*pixel, 6*pixel, 5*layer);
   }
}
module breaks (){
   for(i=[0:2]) {
      translate ([575*pixel+650*pixel*i,0,-100*pixel])
      featureX(100*pixel, 2000*pixel, 300*layer);
   }
}
difference() {
   bulk();
   all_channels() ;
   breaks();
//polymerization window 6 layer
   translate([-150*pixel,850*pixel,51*layer])color("red")cube([4000*pixel,80*pixel,500*layer]);
}
```

A 1.3 Representative Water Contact Angle Picture

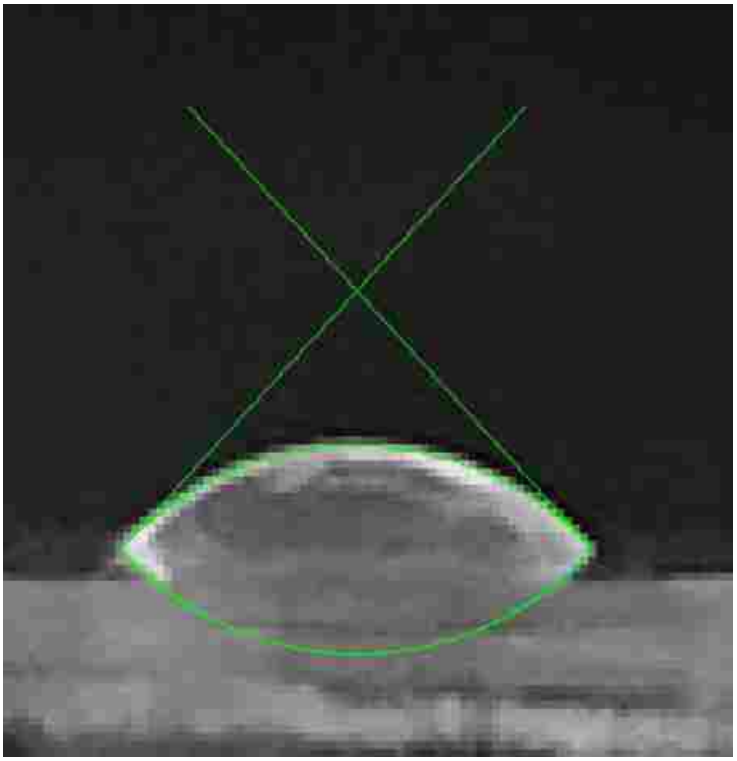

A 1.4 Representative CCD Images for Extractions

A 1.4.1 Extraction of Ferritin

(A) Blank (B) Load (C) Rinse 1 (D) Rinse 2 (E) Elute

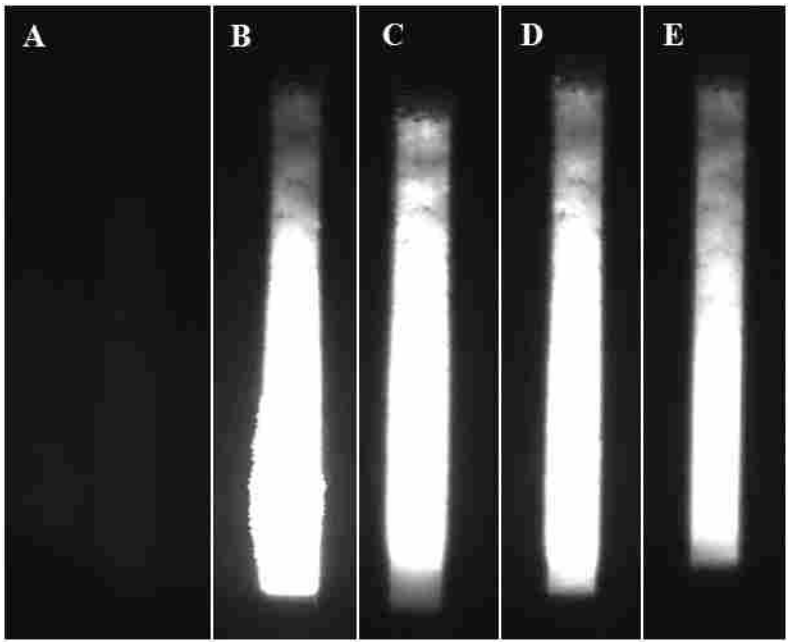

A 1.4.2 Confirmation of Ferritin Selectivity

(A) Blank (B) Load (C) Rinse 1 (D) Rinse 2 (E) Elute

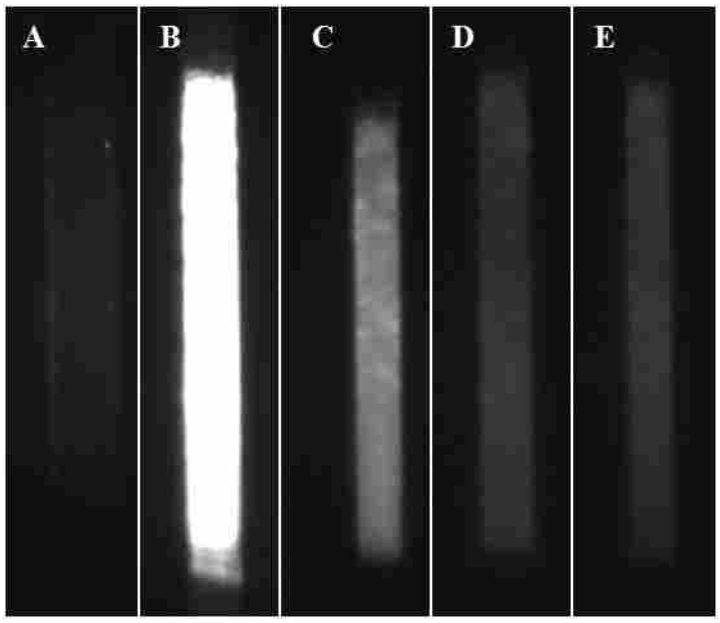

A 1.4.3 Extraction of Ferritin from a Human Blood Sample

(A) Blank (B) Load (C) Rinse 1 (D) Rinse 2 (E) Elute